Chiral spin-wave edge modes in dipolar magnetic thin films

Ryuichi Shindou,[1,2] Jun-ichiro Ohe,[3] Ryo Matsumoto,[1] Shuichi Murakami,[1] and Eiji Saitoh[4]
[1]*Department of Physics, Tokyo Institute of Technology, 2-12-1 Ookayama, Meguro-ku, Tokyo 152-8551, Japan*
[2]*International Center for Quantum Materials, Peking University, No. 5 Yiheyuan Road, Haidian District, Beijing 100871, China*
[3]*Department of Physics, Toho University, 2-2-1 Miyama, Funabashi, Chiba, Japan*
[4]*Institute for Materials Research, Tohoku University, Sendai 980-8557, Japan*
(Received 6 March 2013; revised manuscript received 15 April 2013; published 2 May 2013)

Based on a linearized Landau-Lifshitz equation, we show that two-dimensional periodic allay of ferromagnetic particles coupled with magnetic dipole-dipole interactions supports chiral spin-wave edge modes, when subjected under the magnetic field applied perpendicular to the plane. The mode propagates along a one-dimensional boundary of the system in a unidirectional way and it always has a chiral dispersion within a band gap for spin-wave volume modes. Contrary to the well-known Damon-Eshbach surface mode, the sense of the rotation depends not only on the direction of the field but also on the strength of the field; its chiral direction is generally determined by the sum of the so-called Chern integers defined for spin-wave volume modes below the band gap. Using simple tight-binding descriptions, we explain how the magnetic dipolar interaction endows spin-wave volume modes with nonzero Chern integers and how their values will be changed by the field.

DOI: 10.1103/PhysRevB.87.174402 PACS number(s): 85.75.−d, 85.70.Ec, 73.43.−f, 75.78.Cd

I. INTRODUCTION

Spin waves are collective propagations of precessional motions of magnetic moments in magnetic materials. Magnonics research investigates how the spin wave propagates in the submicrometer length scale and subnanosecond time scale.[1–6] Particularly, the propagation of spin waves in periodically nanostructured magnetic materials dubbed as magnonic crystals[7–10] are one of its central interests. Owing to the periodic structurings, the spin-wave spectrum in magnonic crystal acquires allowed frequency bands of spin-wave modes and forbidden-frequency bands dubbed as magnonic band gap.[7] Similar to other solid-state engineering such as electronics, photonics, and plasmonics, the main application direction is to explore the ability of spin waves to carry and process information. Compared to others, magnonics has a much better prospect for miniaturization of the device because the velocity of a spin wave is typically several orders slower than those of light and electrons in solids.

Recently, the authors proposed a spin-wave analog of the integer quantum Hall (IQH) state,[11] which has unidirectional edge modes for spin-wave propagation. The IQH state is a two-dimensional electron system with broken time-reversal symmetry, which supports unidirectional electric conducting channels along the boundaries (edges) of the system.[12] The number of the unidirectional (chiral) edge modes is determined by a certain kind of topological number defined for *bulk* electron states, called the first Chern integer.[13–15] Based on a linearized Landau-Lifshitz equation, we have generalized the Chern integer well established in quantum Hall physics into the context of spin-wave physics, to argue that a nonzero Chern integer for spin-wave *volume-mode* bands results in an emergence of chiral spin-wave edge modes.[11]

The proposed edge mode has a chiral dispersion with a band gap for volume-mode bands, which supports a unidirectional propagation of spin degree of freedom for a frequency within the gap. The sense of rotation and the number of the chiral mode is determined by the topological number for volume-mode bands below the gap, which itself can be changed by closing the band gap. These features allow us control the chiral edge modes in terms of band-gap manipulation, which could realize novel spintronic devices such as spin current splitters and spin-wave logic gates.[11] To have these devices in real experimental systems, however, it is quite important to have a number of actual magnonic crystals, in which spin-wave volume mode bands take various nonzero Chern integers.

From its electron analog,[16,17] it is expected that finite Chern integers for spin-wave volume-mode bands result from strong spin-orbit-coupled interactions, such as magnetic dipole-dipole interaction. Namely, having an inner product between spin operator and coordinate operator, the magnetic dipolar interaction locks the relative rotational angle between the spin space and orbital space, just in the same way as the relativistic spin-orbit interaction does in electron systems.[16,17] As a result of the spin-orbit locking, the complex-valued character in the spin space (i.e., one of the three Pauli matrices) is transferred into wave functions in the orbital space. Specifically, in the presence of finite out-of-plane ferromagnetic moments in the spin space, the symmetry argument allows the Chern integer for volume-mode bands to have nonzero integer value. In the recent work, employing a standard plane-wave theory, we have shown that a two-dimensional (x-y) bi-component magnonic crystal under an out-of-plane field (along the z direction) acquires spin-wave volume-mode bands with nonzero Chern integers, when magnetic dipolar interaction dominates over short-ranged isotropic exchange interaction. From the state-of-art nanotechnology, however, it is not easy to synthesize the proposed bicomponent magnonic crystal experimentally. Moreover, the proposed model is not simple enough to see how magnetic dipolar interaction leads to nonzero Chern integers for spin-wave volume-mode bands.

In the present paper, we introduce much simpler thin-film magnetic models, which also support spin-wave volume modes with nonzero Chern integers and chiral spin-wave edge modes, under the field normal to the two-dimensional plane. Based on the models, we show that the chiral edge modes have frequency-wavelength dispersions within a band gap for spin-wave volume modes, and their chiral directions are determined by a sign of the Chern integer for a spin-wave

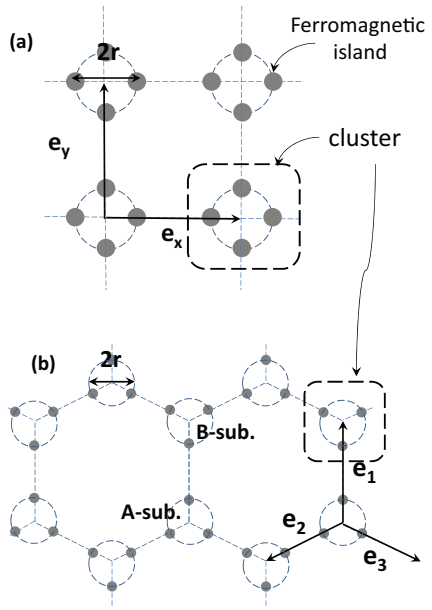

FIG. 1. (Color online) Periodic array of ferromagnetic islands (gray circles) (a) decorated square-lattice model. (b) decorated honeycomb-lattice model. Each gray point stands for a ferromagnetic island (volume element is ΔV), which we assume to behave as a single big spin whose moment is fully saturated (M_s). The spins are coupled via magnetic dipole-dipole interaction. We took $|\boldsymbol{e}_x| = |\boldsymbol{e}_y| = 2.4$, $2r = 1.2, \Delta V = 1.70$, and $M_s = 1.0$ for the square-lattice case, while $|\boldsymbol{e}_1| = |\boldsymbol{e}_2| = |\boldsymbol{e}_3| = 2.4$, $2r = 1.2$, $\Delta V = 1.0$, and $M_s = 1.0$ for the honeycomb-lattice case. The primitive translational vectors $\boldsymbol{a}_\mu$ ($\mu = x, y$) are defined as $\boldsymbol{a}_x = \boldsymbol{e}_x$ and $\boldsymbol{a}_y = \boldsymbol{e}_y$ for the square-lattice model and as $\boldsymbol{a}_x = \boldsymbol{e}_3 - \boldsymbol{e}_2$ and $\boldsymbol{a}_y = \boldsymbol{e}_1 - \boldsymbol{e}_2$ for the honeycomb-lattice case (see text).

volume mode below the gap. Using a simple tight-binding model composed of atomic orbitals, we further argue that the level inversion between the parity-odd atomic orbital (such as p-wave orbital) and parity-even atomic orbital (such as s-wave orbital) leads to a band inversion, which endows spin-wave volume-mode bands with nonzero Chern integers. We expect that these findings would give useful prototype models for future designing of more realistic magnonic crystals, which support topological chiral spin-wave edge modes.

The organization of the paper is as follows. In the next two sections, we introduce the models studied in this paper (Sec. II and Fig. 1), formulate our problem and summarize a calculation procedure of spin-wave band dispersions and the topological Chern integers (Sec. III). In Sec. IV, we show how chiral spin-wave edge modes appear and how they change their directions on increasing the field. The results show that the sense of the rotation of chiral edge mode is indeed determined by the sign of the Chern integer defined for the spin-wave volume mode. In Sec. V, we introduce a tight-binding description of linearized Landau-Lifshitz equations in the context of the present models. In Sec. V A, we first clarify spin-wave excitations within a unit cell in terms of a total angular momentum variable. Based on the atomic orbitals thus obtained, we construct a tight-binding model for a square-lattice model (Sec. V B) and for a honeycomb-lattice model (Sec. V C). Using this tight-binding model, we explain how a level inversion between different atomic-orbital levels leads to an *inverted* spin-wave band with nonzero Chern integers and how the signs of the Chern integers are changed as a function of the field. To see how the proposed chiral spin-wave edge modes could be seen in experiments, we simulate the Landau-Lifshitz-Gilbert equation for the square-lattice model near the saturation field (Sec. VI). Section VII is devoted to a summary and future open issues, in which we also discuss the effects of disorders associated with lattice periodicity and shape of the boundaries.

II. MODEL

In this paper, we consider two-dimensional periodic arrays of ferromagnetic islands. We assume that each ferromagnetic island behaves as a single spin and ferromagnetic islands are coupled via magnetic dipolar interaction. In fact, two-dimensional periodic lattice structures composed of submicrometer-scale ferromagnetic islands have been fabricated experimentally, in which they confirm that each island behaves as a giant single spin under some circumstances.[18,19]

To have volume-mode bands with finite Chern integers, we generally need multiple-band degrees of freedom within a unit cell of magnonic crystal. To this end, we consider two models; the decorated square-lattice model and the honeycomb-lattice model (see Fig. 1). A basic building block of both models is a cluster of ferromagnetic islands. For the decorated square lattice model, four ferromagnetic islands form a circle-shape cluster, which encompasses a site of the square lattice. For the decorated honeycomb-lattice model, three neighboring islands form a circle, which encompasses either an A-sublattice site or a B-sublattice site of the honeycomb lattice.

Experimentally speaking, it is also quite likely that a submicrometer-scale ferromagnetic island has a number of low-energy excitation modes having different spin textures within the island. Such modes can be also regarded as multiple-band degrees of freedom, so that a system with only one ferromagnetic island within a unit cell of magnonic crystal[19] could also have a chance to provide volume mode bands with finite Chern integers and associated chiral edge modes. We expect that the theoretical results obtained in the present model study would also provide useful starting points for further studies on such systems.[20]

III. FORMULATION

For the models introduced above, we first determine a classical spin configuration, which minimizes the following magnetostatic energy:

$$E = -\frac{1}{2}(\Delta V)^2 \sum_{i,j}^{i\neq j} M_a(\boldsymbol{r}_i) f_{ab}(\boldsymbol{r}_i - \boldsymbol{r}_j) M_b(\boldsymbol{r}_j) + H\Delta V \sum_i M_z(\boldsymbol{r}_j), \quad (1)$$

where $\boldsymbol{r}_i$ specifies a spatial location of a ferromagnetic island (classical spin). For simplicity, the norm of each spin is fixed; $|\boldsymbol{M}(\boldsymbol{r}_j)| = M_s$. The magnetic dipole-dipole interaction

is given by a 3×3 matrix,

$$f_{ab}(\boldsymbol{r}) = \frac{1}{4\pi}\left(\frac{\delta_{a,b}}{|\boldsymbol{r}|^3} - \frac{3r_a r_b}{|\boldsymbol{r}|^5}\right) \tag{2}$$

with $a,b = x,y,z$. The summation over i,j in Eq. (1) are taken over all ferromagnetic islands, while the summations over $a,b = x,y,z$ were omitted. A corresponding Landau-Lifshitz equation reads

$$\partial_t M_a(\boldsymbol{r}_i) = \epsilon_{abc}\left[H\delta_{b,z} - \Delta V \sum_{j\neq i} f_{bd}(\boldsymbol{r}_i - \boldsymbol{r}_j) M_d(\boldsymbol{r}_j)\right] M_c(\boldsymbol{r}_i). \tag{3}$$

ΔV is a volume element for each ferromagnetic island. From dimensional analysis, one can see that a saturation field and resonance frequency of spin-wave excitations are scaled by $M_s \Delta V / l^3$, where l is a characteristic length scale for the periodic structuring within the two-dimensional plane, e.g., radius (r) of the circle-shape M-spin cluster. In the following, we take this value to be around 1; $M_s = 1, \Delta V = 1.0, 2r = 1.2$ for the square-lattice case and $M_s = 1$, $\Delta V = 1.7$, $2r = 1.2$ for the honeycomb-lattice case.

A. Classical spin configuration

1. Square-lattice model

For the decorated square-lattice case, we found that every four spins within a circle-shape cluster form a same vortex,

$$M_0\left[\boldsymbol{r} = r\left(c_{\theta_j}, s_{\theta_j}\right)\right] = M_s\left(-s_\varphi s_{\theta_j}, s_\varphi c_{\theta_j}, c_\varphi\right), \tag{4}$$

with $\theta_j \equiv \frac{2\pi j}{4}$ ($j = 1,\ldots,4$) and $(s_\theta, c_\theta) \equiv (\sin\theta, \cos\theta)$, such that the classical spin configuration $\boldsymbol{M}_0(\boldsymbol{r})$ respects the translational symmetries of the square lattice, $\boldsymbol{M}_0(\boldsymbol{r} + \boldsymbol{a}_\mu) = \boldsymbol{M}_0(\boldsymbol{r})$ (see Fig. 2). A finite out-of-plane component ($\varphi \neq \frac{\pi}{2}$) is induced by the field. Above the saturation field ($H > H_c = 1.71$), all the spins become fully polarized along the field ($\varphi = \pi$).

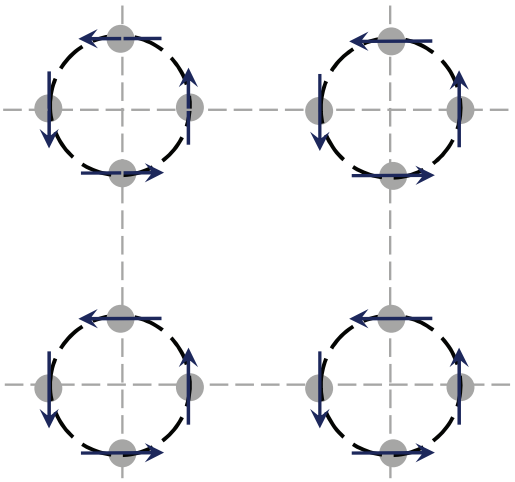

FIG. 2. (Color online) Top view of classical spin configurations for the decorated square-lattice model. The field is lower than the saturation field, so that spins have finite in-plane components, forming a vortex structure.

2. Honeycomb-lattice model

For the decorated honeycomb-lattice case, the classical spin configuration below a saturation field ($H < H_c = 0.57$) breaks the translational symmetries of the lattice, while that above the field is a fully polarized state respecting the translational symmetries of the honeycomb lattice. For simplicity, we only consider spin-wave excitations above the saturation field for the decorated honeycomb-lattice case.

B. Linearized Landau-Lifshitz equation

Starting from the classical spin configurations thus obtained, $\boldsymbol{M}_0(\boldsymbol{r})$, the Landau-Lifshitz equation is linearized with respect to a small transverse fluctuation field $\boldsymbol{m}_\perp(\boldsymbol{r})$, with $\boldsymbol{M}(\boldsymbol{r}) \equiv \boldsymbol{M}_0(\boldsymbol{r}) + \boldsymbol{m}_\perp(\boldsymbol{r})$ and $\boldsymbol{m}_\perp \perp \boldsymbol{M}_0$. In terms of a rotated frame with a 3×3 rotational matrix $\boldsymbol{R}(\boldsymbol{r})$, with which $\boldsymbol{M}_0(\boldsymbol{r})$ is always pointing along the z direction, $\boldsymbol{R}(\boldsymbol{r})\boldsymbol{M}_0(\boldsymbol{r}) \equiv M_s \boldsymbol{e}_z$ and $\boldsymbol{R}(\boldsymbol{r})\boldsymbol{m}_\perp(\boldsymbol{r}) \equiv \boldsymbol{m}(\boldsymbol{r})$, the linearized equation of motion for the transverse moments takes the form

$$-\partial_t m_\mu(\boldsymbol{r}_i) = \epsilon_{\mu\nu}\alpha(\boldsymbol{r}_i) m_\nu(\boldsymbol{r}_i) + M_s \Delta V\, \epsilon_{\mu\nu} \sum_{j\neq i} f_{\nu\lambda}(\boldsymbol{r}_i, \boldsymbol{r}_j) m_\lambda(\boldsymbol{r}_j), \tag{5}$$

where $\boldsymbol{m} \equiv (m_x, m_y, 0)$ and the summation over the repeated indices μ,ν,λ are taken only over x,y with $\epsilon_{xy} = -\epsilon_{yx} = 1$. The first term in the right-hand side includes a demagnetization field and the external field

$$\alpha(\boldsymbol{r}_i)\boldsymbol{M}_0(\boldsymbol{r}_i) = -\Delta V \sum_{j\neq i} \boldsymbol{f}(\boldsymbol{r}_i - \boldsymbol{r}_j)\boldsymbol{M}_0(\boldsymbol{r}_j) + H\boldsymbol{e}_z,$$

where, provided that $\boldsymbol{M}_0(\boldsymbol{r}_j)$ gives a local minimum for the magnetostatic energy Eq. (1), the equality always holds true for a certain scalar function $\alpha(\boldsymbol{r}_i)$. The dipole-dipole interaction in the second term of Eq. (5) is given in the rotated frame

$$\boldsymbol{f}(\boldsymbol{r}_i, \boldsymbol{r}_j) \equiv \boldsymbol{R}(\boldsymbol{r}_i)\boldsymbol{f}(\boldsymbol{r}_i - \boldsymbol{r}_j)\boldsymbol{R}^t(\boldsymbol{r}_j).$$

In terms of $m_\pm \equiv m_x \pm i m_y$, which are magnon creation/annihilation fields, respectively, the equation of motion reduces to a following form:

$$-i\partial_t \boldsymbol{\sigma}_3 \begin{pmatrix} m_+(\boldsymbol{r}_i) \\ m_-(\boldsymbol{r}_i) \end{pmatrix} = \alpha(\boldsymbol{r}_i) M_s \begin{pmatrix} m_+(\boldsymbol{r}_i) \\ m_-(\boldsymbol{r}_i) \end{pmatrix} + M_s \Delta V \times \sum_{j\neq i} \begin{pmatrix} f_{++}(\boldsymbol{r}_i, \boldsymbol{r}_j) & f_{+-}(\boldsymbol{r}_i, \boldsymbol{r}_j) \\ f_{-+}(\boldsymbol{r}_i, \boldsymbol{r}_j) & f_{--}(\boldsymbol{r}_i, \boldsymbol{r}_j) \end{pmatrix} \begin{pmatrix} m_+(\boldsymbol{r}_j) \\ m_-(\boldsymbol{r}_j) \end{pmatrix}, \tag{6}$$

where a 2×2 diagonal Pauli matrix $\boldsymbol{\sigma}_3$ takes $+1$ for the creation field (particle space), while taking -1 for the annihilation field (hole space). A Green's function $f_{\alpha\beta}(\boldsymbol{r}, \boldsymbol{r}')$ ($\alpha,\beta = \pm$) in the second term takes a form of a certain Hermite matrix in the particle-hole space,

$$\begin{pmatrix} f_{++}(\boldsymbol{r}, \boldsymbol{r}') & f_{+-}(\boldsymbol{r}, \boldsymbol{r}') \\ f_{-+}(\boldsymbol{r}, \boldsymbol{r}') & f_{--}(\boldsymbol{r}, \boldsymbol{r}') \end{pmatrix} = \frac{1}{2}\begin{pmatrix} 1 & i \\ 1 & -i \end{pmatrix} \begin{pmatrix} f_{xx}(\boldsymbol{r}, \boldsymbol{r}') & f_{xy}(\boldsymbol{r}, \boldsymbol{r}') \\ f_{yx}(\boldsymbol{r}, \boldsymbol{r}') & f_{yy}(\boldsymbol{r}, \boldsymbol{r}') \end{pmatrix} \begin{pmatrix} 1 & 1 \\ -i & i \end{pmatrix},$$

with $f^*_{\alpha\beta}(\boldsymbol{r},\boldsymbol{r}') = f_{\beta\alpha}(\boldsymbol{r}',\boldsymbol{r})$. Accordingly, the problem reduces to solving the following generalized eigenvalue problem:

$$\sum_j (\boldsymbol{H})_{\boldsymbol{r}_i,\boldsymbol{r}_j} \begin{pmatrix} m_+(\boldsymbol{r}_j) \\ m_-(\boldsymbol{r}_j) \end{pmatrix} = \boldsymbol{\sigma}_3 \begin{pmatrix} m_+(\boldsymbol{r}_i) \\ m_-(\boldsymbol{r}_i) \end{pmatrix} \overline{E} \tag{7}$$

with a Hermite matrix $\boldsymbol{H}$,

$$(\boldsymbol{H})_{\boldsymbol{r}_i,\boldsymbol{r}_j} = -M_s \alpha(\boldsymbol{r}_i)\delta_{\boldsymbol{r}_i,\boldsymbol{r}_j} \begin{pmatrix} 1 & \\ & 1 \end{pmatrix} - M_s \Delta V \left(1 - \delta_{\boldsymbol{r}_i,\boldsymbol{r}_j}\right) \times \begin{pmatrix} f_{++}(\boldsymbol{r}_i,\boldsymbol{r}_j) & f_{+-}(\boldsymbol{r}_i,\boldsymbol{r}_j) \\ f_{-+}(\boldsymbol{r}_i,\boldsymbol{r}_j) & f_{--}(\boldsymbol{r}_i,\boldsymbol{r}_j) \end{pmatrix}. \tag{8}$$

The sum of j is taken over all spins in the systems. Using the Cholesky decomposition,[21] the Hermite matrix can be diagonalized by a paraunitary transformation matrix $\boldsymbol{T}$

$$\boldsymbol{H}\boldsymbol{T} = \boldsymbol{\sigma}_3 \boldsymbol{T} \overline{\boldsymbol{E}} \tag{9}$$

with a proper normalization condition $\boldsymbol{T}^\dagger \boldsymbol{\sigma}_3 \boldsymbol{T} = \boldsymbol{\sigma}_3$ and a diagonal matrix $\overline{\boldsymbol{E}}$.

Now that the saddle-point solution respects the translational symmetries, $\boldsymbol{M}_0(\boldsymbol{r}+\boldsymbol{a}_\mu) = \boldsymbol{M}_0(\boldsymbol{r})$, so does the Green's function and the demagnetization coefficient, $\boldsymbol{f}(\boldsymbol{r}+\boldsymbol{a}_\mu,\boldsymbol{r}') = \boldsymbol{f}(\boldsymbol{r},\boldsymbol{r}'-\boldsymbol{a}_\mu)$ and $\alpha(\boldsymbol{r}+\boldsymbol{a}_\mu) = \alpha(\boldsymbol{r})$ with the primitive translational vectors $\boldsymbol{a}_\mu$ ($\mu = x,y$). Moreover, the classical spin configuration Eq. (4) is invariant under the simultaneous C_4 rotations in the spin space and the lattice space (around z axis), so that the demagnetization coefficient within a unit cell has no spatial dependence, $\alpha(\boldsymbol{r}_j) = \alpha$. This also holds true for the honeycomb-lattice case considered.

With the Born-von Karman boundary condition, the eigenvalue problem reduces to a diagonalization of following Bogoliubov-de Gennes (BdG) type Hamiltonian for every crystal momentum $\boldsymbol{k} = (k_x,k_y)$:

$$i\partial_t \boldsymbol{\sigma}_3 \begin{pmatrix} u_{+,\boldsymbol{k}}(\boldsymbol{r}_i) \\ u_{-,-\boldsymbol{k}}(\boldsymbol{r}_i) \end{pmatrix} = \sum_{j=1}^{M_U} (\boldsymbol{H}_{\boldsymbol{k}})_{\boldsymbol{r}_i,\boldsymbol{r}_j} \begin{pmatrix} u_{+,\boldsymbol{k}}(\boldsymbol{r}_j) \\ u_{-,-\boldsymbol{k}}(\boldsymbol{r}_j) \end{pmatrix}$$

with

$$(\boldsymbol{H}_{\boldsymbol{k}})_{\boldsymbol{r}_i,\boldsymbol{r}_j} \equiv -M_s \alpha \delta_{\boldsymbol{r}_i,\boldsymbol{r}_j} - M_s \Delta V \begin{pmatrix} f_{\boldsymbol{k},++}(\boldsymbol{r}_i,\boldsymbol{r}_j) & f_{\boldsymbol{k},+-}(\boldsymbol{r}_i,\boldsymbol{r}_j) \\ f_{\boldsymbol{k},-+}(\boldsymbol{r}_i,\boldsymbol{r}_j) & f_{\boldsymbol{k},--}(\boldsymbol{r}_i,\boldsymbol{r}_j) \end{pmatrix}, \tag{10}$$

and

$$f_{\boldsymbol{k},\alpha\beta}(\boldsymbol{r},\boldsymbol{r}') \equiv e^{-i\boldsymbol{k}(\boldsymbol{r}-\boldsymbol{r}')} \sum_{\boldsymbol{b}} (1 - \delta_{\boldsymbol{r},\boldsymbol{r}'-\boldsymbol{b}}) f_{\alpha\beta}(\boldsymbol{r},\boldsymbol{r}'-\boldsymbol{b}) e^{-i\boldsymbol{k}\boldsymbol{b}},$$

and

$$m_\pm(\boldsymbol{r}+\boldsymbol{a}_\mu) \equiv \sum_{\boldsymbol{k}} e^{\pm i\boldsymbol{k}\boldsymbol{a}_\mu} u_{\pm,\boldsymbol{k}}(\boldsymbol{r}).$$

The summation with respect to j (or $\boldsymbol{r}_j$) in the right-hand side is taken over a unit cell. For decorated square and honeycomb lattice, $M_U = 4$ and 6 respectively. The summation over the translation vectors $\boldsymbol{b}$ are taken over sufficiently many unit cells in actual numerical calculations, $\boldsymbol{b} = n\boldsymbol{a}_x + m\boldsymbol{a}_y$ with $-50 \leqslant n,m \leqslant 50$. In terms of the Cholesky decomposition, the $2M_U \times 2M_U$ BdG Hamiltonian is diagonalized

$$\boldsymbol{H}_{\boldsymbol{k}} |\psi_j\rangle = \boldsymbol{\sigma}_3 |\psi_j\rangle \overline{E}_{j,\boldsymbol{k}} \tag{11}$$

with the normalization condition, $\langle\psi_j|\boldsymbol{\sigma}_3|\psi_j\rangle = (-1)^{\sigma_j}$, where $\sigma_j = 0$ for particle bands, $j = 1,\ldots,M_U$, and $\sigma_j = 1$ for hole bands $j = M_U+1,\ldots,2M_U$. Provided that the spin-wave Hamiltonian is derived from an energy minimum of the magnetostatic energy Eq. (1), it is guaranteed that eigenvalues for particle bands ($j = 1,\ldots,M$) are positive definite $\overline{E}_{j,\boldsymbol{k}} > 0$ for any $\boldsymbol{k}$, while those for the hole bands($j = M_U+1,\ldots,2M_U$) are all negative, $\overline{E}_{j,\boldsymbol{k}} < 0$ for any $\boldsymbol{k}$. In fact, this is true for all the cases studied in this paper.

The eigenvalues in the particle bands, $\overline{E}_{j,\boldsymbol{k}}$ ($j = 1,\ldots,M_U$), determine wavelength-frequency dispersion relations for all the spin-wave volume-mode bands. An eigenvector, $|\psi_j\rangle$, is a Bloch wave function for the corresponding spin-wave volume-mode band. In terms of the Bloch wave function, we have calculated the first Chern integer defined for each spin-wave band as,[11]

$$\begin{aligned} \mathrm{Ch}_j &\equiv i(-1)^{\sigma_j} \epsilon_{\mu\nu} \int_{\mathrm{BZ}} d^2\boldsymbol{k} \left\langle \partial_{k_\mu}\psi_j \middle| \boldsymbol{\sigma}_3 \middle| \partial_{k_\nu}\psi_j \right\rangle \\ &= i \sum_{m=1,\ldots,2M_U}^{m\neq j} \int_{\mathrm{BZ}} d^2\boldsymbol{k} \frac{(-1)^{\sigma_j}(-1)^{\sigma_m}}{(\overline{E}_{j,\boldsymbol{k}} - \overline{E}_{m,\boldsymbol{k}})^2} \\ &\quad \times \left\{ \langle\psi_j| \frac{\partial \boldsymbol{H}_{\boldsymbol{k}}}{\partial k_x} |\psi_m\rangle \langle\psi_m| \frac{\partial \boldsymbol{H}_{\boldsymbol{k}}}{\partial k_y} |\psi_j\rangle - (x \leftrightarrow y) \right\}. \end{aligned} \tag{12}$$

Contrary to the Chern integer defined for an electron's wave function,[13] Eq. (12) contains the diagonal Pauli matrix $\boldsymbol{\sigma}_3$ between bra state and ket state, which takes $+1$ in the particle space while -1 in the hole space. This additional structure comes from the fact that magnon obeys the boson statistics,[11] which enforces the respective BdG Hamiltonian such as Eqs. (8) and (10) to be diagonalized in terms of a paraunitary matrix instead of a unitary matrix. Due to this paraunitary character in the particle-hole space, we can also argue that the sum of the magnonic Chern integer over all *particle* bands always reduce to zero, $\sum_{j=1}^{M_U} \mathrm{Ch}_j = 0$, which leads to the absence of *gapless* topological chiral spin-wave edge mode.[11]

In the next section, we have calculated spin-wave excitations with the open boundary condition along one direction (y direction) while the periodic boundary condition along the other (x direction); the frequency-wavelength dispersions for the spin-wave edge modes are obtained as a function of (surface) momentum along the x direction, k_x. The dispersions thus obtained allow us to see the propagation direction of the chiral spin-wave edge mode. With changing the strength of the field, we have calculated spin-wave band dispersions for both volume modes and edge modes and the Chern integer for all the volume modes.

IV. RESULTS

A. Square-lattice model

Results for the square-lattice model are summarized in Figs. 3, 4, and 5. Without the field, the system has no magnetization perpendicular to the plane, so that the spin-wave Hamiltonian respects both time-reversal symmetry, $\boldsymbol{H}_{-\boldsymbol{k}} = \boldsymbol{H}^*_{\boldsymbol{k}}$, and mirror symmetries, e.g., $\boldsymbol{H}_{(k_x,k_y)} = \boldsymbol{H}_{(k_x,-k_y)}$. The Chern integer for all the four bands are required to be zero by these symmetries [Fig. 3(a)], and no chiral spin-wave edge

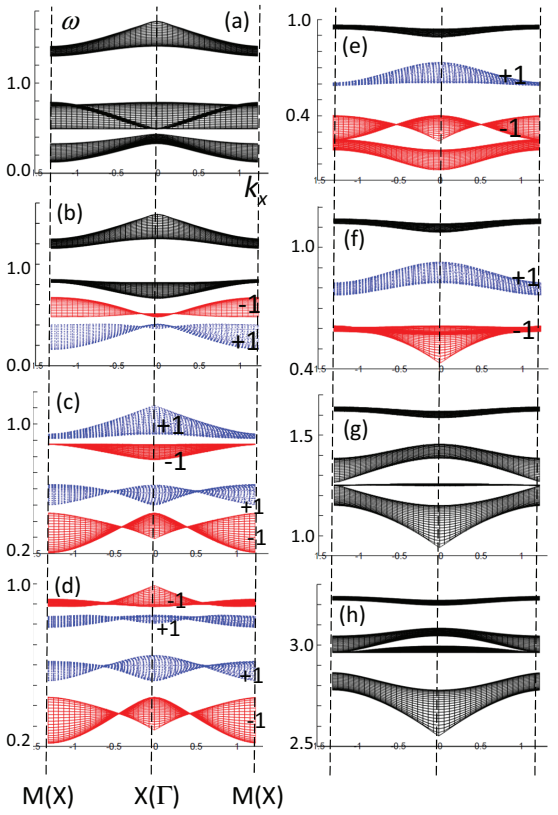

FIG. 3. (Color online) (a)–(d) Side view of wavelength-frequency dispersions of four spin-wave volume-mode bands in the square lattice model under fields (H) normal to the two-dimensional plane; (a) $H = 0.0$, (b) $H = 0.47H_c$, (c) $H = 0.76H_c$ (d) $H = 0.82H_c$, (e) $H = 1.01H_c$, (f) $H = 1.1H_c$, (g) $H = 1.4H_c$, and (h) $H = 2.35H_c$ where $H_c = 1.71$. The Chern integer for red/blue-colored spin-wave bands is $-1/+1$, while 0 otherwise.

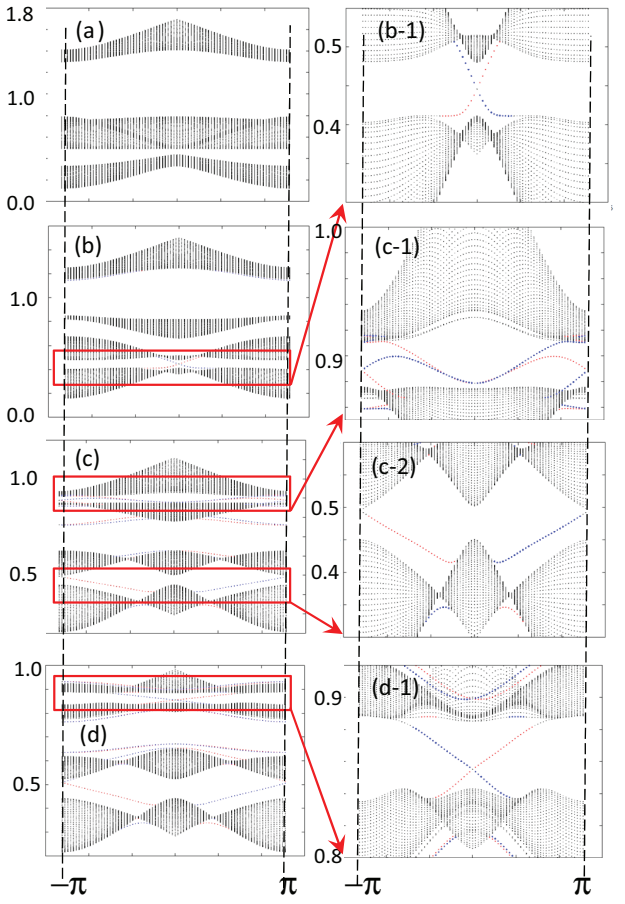

FIG. 4. (Color online) (a)–(d) Wavelength-frequency dispersions calculated with open boundary condition along one direction (y direction) and periodic boundary condition along the other (decorated square-lattice model); (a) $H = 0.0$; (b), (b-1) $H = 0.47H_c$; (c), (c-1), (c-2) $H = 0.76H_c$; (d), (d-1) $H = 0.82H_c$ with $H_c = 1.71$. The system along the y direction includes 40 unit cells ($L = 40$). More than 80% of wave functions for red-colored points are localized from $y = L - 3$ to $y = L$, while those for blue-colored points are localized from $y = 1$ to $y = 4$. Compared with Figs. 3(a)–3(d), spectra are comprised also of edge-mode bands, whose chiral dispersions runs across band gaps for spin wave volume modes.

modes are observed [Fig. 4(a)]. With the field along the z direction, these symmetries are gone.

On increasing the field, there appears a sequence of band touchings between the lowest spin-wave band and the second lowest one at the Γ point ($H = 0.24H_c$) and two inequivalent X points ($H = 0.67H_c$). As a result of these band touchings, the Chern integers for the lowest band and the second lowest one become $+1$ and -1, respectively for $0.24 < H/H_c < 0.67$ [Fig. 3(b)], -1 and $+1$ respectively for $0.67 < H/H_c$ [Figs. 3(c) and 3(d)]. Correspondingly, there appears a chiral spin-wave edge mode propagating in the clockwise direction for $0.24 < H/H_c < 0.67$, whose dispersion runs across a band gap between these two spin-wave volume-mode bands [Figs. 4(b) and 4(b-1)]. When the band gap closes and reopens at $H/H_c = 0.67$, the chiral spin-wave edge mode changes its direction from clockwise to anticlockwise [Figs. 4(c) and 4(c-2)]. The anticlockwise edge mode remains for a relatively larger range of the field strength, $0.67 < H/H_c < 1.4$ [Figs. 4(d), 5(a), 5(b), 5(a-1), and 5(b-1)] .

There is also another sequence of band touchings between the third lowest spin-wave band and the highest one. They appear at $H = 0.71H_c$ (M point), $H = 0.79H_c$ (two inequivalent X points) and $H = 0.85H_c$ (Γ point). Correspondingly, the first Chern integers for the third lowest band and the highest band become -1 and $+1$ for $0.71 < H/H_c < 0.79$ [Fig. 3(c)], $+1$ and -1 for $0.79 < H/H_c < 0.85$ [Fig. 3(d)], while 0 otherwise. They lead to a chiral spin-wave edge mode with anticlockwise propagation [$0.71 < H/H_c < 0.79$, Figs. 4(c) and 4(c-1)] and that with clockwise propagation [$0.79 < H/H_c < 0.85$, Figs. 4(d) and 4(d-1)] between these two volume-mode bands.

In the limit of strong field, the system becomes effectively time-reversal symmetric, $\boldsymbol{H}_{\boldsymbol{k}}^{*} = \boldsymbol{H}_{-\boldsymbol{k}}$ (consult also a perturbation analysis presented in Sec. IV C), where the Chern integers for all the four spin-wave volume-mode bands reduce to zero and the system does not support any chiral spin-wave edge mode which crosses band gaps for spin-wave volume-mode bands. Yet there still exist spin wave edge modes, which have parabolic dispersions at their lowest (or highest) frequency levels and thus consist of both right-moving modes and

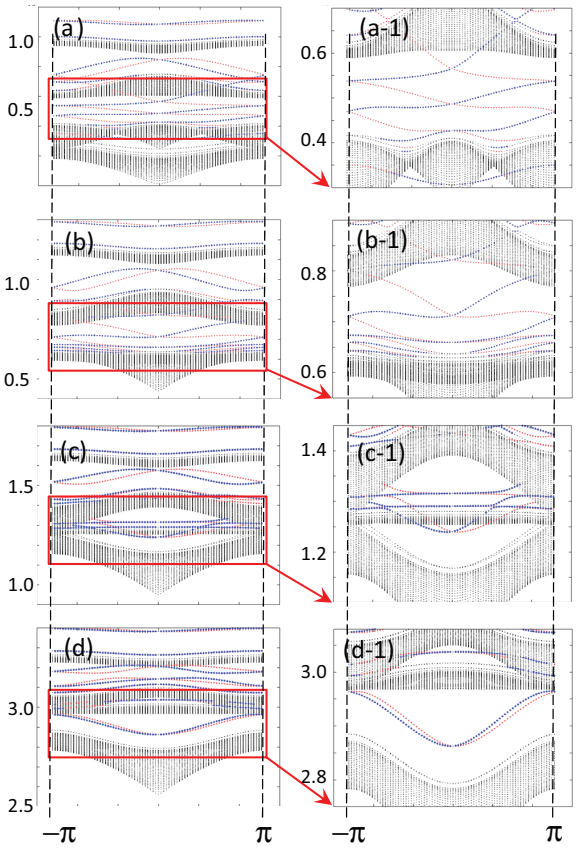

FIG. 5. (Color online) (a)–(d) Wavelength-frequency dispersions calculated with open boundary condition along one direction (y direction) and periodic boundary condition along the other (decorated square-lattice model). (a), (a-1) $H = 1.01H_c$; (b), (b-1) $H = 1.1H_c$; (c), (c-1) $H = 1.4H_c$; (d), (d-1) $H = 2.35H_c$ with $H_c = 1.71$.

left-moving modes on a same side of the boundary [Figs. 5(d) and 5(d-1)].

B. Honeycomb-lattice model

Results for the decorated honeycomb lattice are shown in Fig. 5. Above the saturation field $H \geqslant H_c = 0.57$, the lowest spin-wave volume-mode band and the second lowest one are always separated by a finite band gap. The Chern integers for these two bands are quantized to -1 and $+1$ respectively for $H \geqslant H_c = 0.57$, and a chiral spin-wave edge mode with the anticlockwise propagation cross the band gap between these two [Figs. 6(a) and 6(a-1)]. On increasing the field, the band gap becomes smaller but always remains finite [Figs. 6(b) and 6(b-1)]. Only in the strong field limit, the gap closes and the lowest two bands form two massless Dirac-cone spectra at two inequivalent K points, $\boldsymbol{k} = \boldsymbol{K}$ and $\boldsymbol{K}'$ with $\boldsymbol{K}\cdot\boldsymbol{e}_1 = -\boldsymbol{K}\cdot\boldsymbol{e}_2 = -\boldsymbol{K}'\cdot\boldsymbol{e}_3 = \boldsymbol{K}'\cdot\boldsymbol{e}_1 = \frac{2\pi}{3}$ and $\boldsymbol{K}\cdot\boldsymbol{e}_3 = \boldsymbol{K}'\cdot\boldsymbol{e}_2 = 0$, where the Chern integers for these two bands reduce to zero (see also Sec. IV C). In other words, the band gap and the chiral spin-wave edge mode which crosses over the gap persist even in the presence of large (but finite) field for the decorated honeycomb-lattice model.

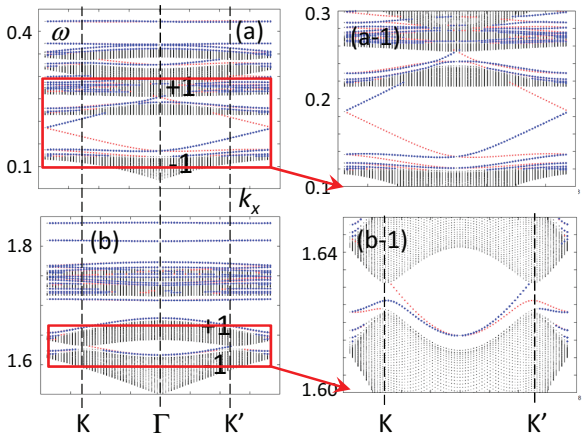

FIG. 6. (Color online) (a)–(b) Wavelength-frequency dispersions calculated with open boundary condition along one direction (y direction) with the zigzag boundary (decorated honeycomb-lattice model). The system along the y direction includes 30 unit cells ($L = 30$). Wave functions for red-colored points are localized from $y = L - 2$ to $y = L$ (>80%), while those for blue-colored points are localized from $y = 1$ to $y = 3$. (a), (a-1) $H = 1.05H_c$; (b), (b-1) $H = 3.5H_c$, where $H_c = 0.57$.

V. TIGHT-BINDING DESCRIPTIONS

Although we are dealing with a classical spin problem, the calculation procedure so far is totally in parallel with what the standard Holstein-Primakoff approximation[22–24] does in localized quantum spin models based on large S expansion (where S denotes the size of a localized quantum spin). Finding a classical spin configuration of a given localized spin model (on the order of S^2; treating spin as a classical spin) corresponds to the minimization of the magnetostatic energy, Eq. (1) (Sec. III A). Reducing a spin model Hamiltonian into a quadratic form in terms of Holstein-Primakoff boson field (on the order of S) corresponds to linearizing the Landau-Lifshitz equation, Eq. (3), around the classical spin configuration (see Sec. III B). In fact, we diagonalized a quadratic form of the spin-wave Hamiltonian, Eq. (8), to obtain frequency levels of spin-wave modes (Sec. IV). A tight-binding (TB) description introduced in this section is one approximate way of doing this diagonalization, which in fact gives useful physical pictures for results obtained in the previous section.

To construct a TB description for Eqs. (6) and (7), let us first decompose the Hamiltonian defined by Eq. (8) into a diagonal part and off-diagonal part with respect to the M-spin cluster index

$$(\boldsymbol{H})_{\boldsymbol{r}_i,\boldsymbol{r}_j} = (\boldsymbol{H}_0)_{\boldsymbol{r}_i,\boldsymbol{r}_j} + (\boldsymbol{H}_1)_{\boldsymbol{r}_i,\boldsymbol{r}_j},$$

with

$$(\boldsymbol{H}_0)_{\boldsymbol{r}_i,\boldsymbol{r}_j} = -M_s\alpha\delta_{\boldsymbol{r}_i,\boldsymbol{r}_j}\begin{pmatrix}1 & \\ & 1\end{pmatrix} - M_s\Delta V\ \delta_{[\boldsymbol{r}_i],[\boldsymbol{r}_j]}\eta_{\boldsymbol{r}_i,\boldsymbol{r}_j} \times \begin{pmatrix} f_{++}(\boldsymbol{r}_i,\boldsymbol{r}_j) & f_{+-}(\boldsymbol{r}_i,\boldsymbol{r}_j) \\ f_{-+}(\boldsymbol{r}_i,\boldsymbol{r}_j) & f_{--}(\boldsymbol{r}_i,\boldsymbol{r}_j)\end{pmatrix}, \tag{13}$$

$$(\boldsymbol{H}_1)_{\boldsymbol{r}_i,\boldsymbol{r}_j} = -M_s\Delta V\ \eta_{[\boldsymbol{r}_i],[\boldsymbol{r}_j]}\begin{pmatrix} f_{++}(\boldsymbol{r}_i,\boldsymbol{r}_j) & f_{+-}(\boldsymbol{r}_i,\boldsymbol{r}_j) \\ f_{-+}(\boldsymbol{r}_i,\boldsymbol{r}_j) & f_{--}(\boldsymbol{r}_i,\boldsymbol{r}_j)\end{pmatrix}, \tag{14}$$

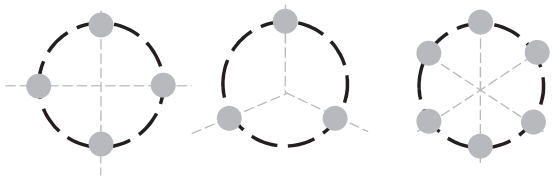

FIG. 7. A single M-spin cluster for $M = 4,3,6$. M spins (gray circle) align along a circle (radius r), taking an equal distance between their nearest-neighbor spins. Each spin has a saturation magnetization (M_s) and a finite volume element (ΔV).

where $\eta_{[\boldsymbol{r}_i],[\boldsymbol{r}_j]} = 1 - \delta_{[\boldsymbol{r}_i],[\boldsymbol{r}_j]}$ and $[\boldsymbol{r}_i]$ specifies an M-spin cluster in which the spin site $\boldsymbol{r}_i$ is included; the four-spin cluster for the decorated square-lattice case ($M = 4$) and the three-spin clusters for the honeycomb-lattice case ($M = 3$); see Fig. 7.

Suppose that $\boldsymbol{H}_0$ is diagonalized in terms of appropriate atomic orbitals localized at each M-spin cluster

$$\boldsymbol{H}_0\boldsymbol{T}_0 = \boldsymbol{\sigma}_3\boldsymbol{T}_0\boldsymbol{\sigma}_3\tilde{\boldsymbol{H}}_0.$$

$\tilde{\boldsymbol{H}}_0$ is a diagonal matrix, whose elements correspond to respective atomic-orbital levels; the column of $\boldsymbol{T}_0$ are specified by atomic-orbital index (j,m), cluster index (n,n'), and particle-hole index (μ,ν). The orthonormal condition for the new basis is given as $\boldsymbol{T}_0^\dagger\boldsymbol{\sigma}_3\boldsymbol{T}_0 = \boldsymbol{\sigma}_3$. In terms of the basis, the original eigenvalue problem, Eq. (11), reduces to

$$(\tilde{\boldsymbol{H}}_0 + \tilde{\boldsymbol{H}}_1)\boldsymbol{S} = \boldsymbol{\sigma}_3\boldsymbol{S}\overline{\boldsymbol{E}}, \tag{15}$$

with $\boldsymbol{T} \equiv \boldsymbol{T}_0\boldsymbol{S}$. The row of $\boldsymbol{S}$ and the row and the column of $\tilde{\boldsymbol{H}}_1$ are specified by atomic orbital (j,m), cluster (n,n') and particle-hole (μ,ν) indices

$$(\tilde{\boldsymbol{H}}_1)_{(j,n,\mu|m,n',\nu)} \equiv (\boldsymbol{T}_0^\dagger\boldsymbol{H}_1\boldsymbol{T}_0)_{(j,n,\mu|m,n',\nu)}, \tag{16}$$

$$(\tilde{\boldsymbol{H}}_0)_{(j,n,\mu|m,n',\nu)} \equiv \delta_{j,m}\delta_{n,n'}\delta_{\mu,\nu}E_{0,j}, \tag{17}$$

where atomic-orbital levels $E_{0,j}$ being positive definite, $E_{0,j} > 0$. By its construction, $\tilde{\boldsymbol{H}}_1$ has a finite matrix element only between atomic orbitals localized at different clusters, which thus stands for interorbital or intraorbital hopping terms between clusters. In terms of the creation/annihilation fields for the jth atomic orbital localized at the nth cluster, $\gamma_{j,n}^\dagger/\gamma_{j,n}$, Eq. (15) takes the form,

$$E_{0,j}\gamma_{j,n} + \sum_m\sum_{n'}(\boldsymbol{t}^{(+,+)}_{(j,n|m,n')}\gamma_{m,n'} + \boldsymbol{t}^{(+,-)}_{(j,n|m,n')}\gamma^\dagger_{m,n'}) = \gamma_{j,n}\overline{E} \tag{18}$$

$$E_{0,j}\gamma^\dagger_{j,n} + \sum_m\sum_{n'}(\boldsymbol{t}^{(-,+)}_{(j,n|m,n')}\gamma_{m,n'} + \boldsymbol{t}^{(-,-)}_{(j,n|m,n')}\gamma^\dagger_{m,n'}) = -\gamma^\dagger_{j,n}\overline{E}, \tag{19}$$

with

$$\boldsymbol{t}^{(\mu,\nu)}_{(j,n|m,n')} \equiv (\boldsymbol{T}_0^\dagger\boldsymbol{H}_1\boldsymbol{T}_0)_{(j,n,\mu|m,n',\nu)}. \tag{20}$$

A. Atomic orbitals

To gain a useful insight on how atomic-orbital levels for $\boldsymbol{H}_0$ behave as a function of the out-of-plane field, let us first calculate eigenmodes for a *single* M-spin cluster formed by M spins; M spins align along a circle such that any neighboring two spins are separated by a same distance (Fig. 7). As an energy minimum of the magnetostatic energy, the M spins form a vortex structure with a finite out-of-plane component,

$$M[\boldsymbol{r}_j = r(c_{\theta_j},s_{\theta_j})] = (-s_\varphi s_{\theta_j}, s_\varphi c_{\theta_j}, c_\varphi) \tag{21}$$

with $\theta_j = \frac{2\pi j}{M}$ $(j = 1,\ldots,M)$ and $(s_\theta,c_\theta) \equiv (\sin\theta,\cos\theta)$. The saturation field is given as $H_c/M_s \equiv 6A_0(0) - 2A_1(0)$ with

$$A_0(0) \equiv \frac{\Delta V}{64\pi r^3}\sum_{j=1}^{M-1}\frac{1}{s^3_{\frac{\theta_j}{2}}}, \quad A_1(0) \equiv \frac{\Delta V}{64\pi r^3}\sum_{j=1}^{M-1}\frac{1}{s_{\frac{\theta_j}{2}}}.$$

ΔV denotes a volume element of each ferromagnetic island (spin) and r is a radius of the circle. For $H < H_c$, $\varphi \equiv \mathrm{Cos}^{-1}[-H/H_c]$ and $\alpha = -4A_0(0) + 2A_1(0)$, while $\varphi = \pi$ and $\alpha = -H/M_s + 2A_0(0)$ for $H > H_c$. Armed with these values, excitation modes are obtained by diagonalizing Eq. (13) with $\boldsymbol{r}_j = r(c_{\theta_j},s_{\theta_j})$ and $\theta_j \equiv \frac{2\pi j}{M}$ $(j = 1,\ldots,M)$. With a proper choice of the $U(1)$ gauge for $m_\pm$

$$\boldsymbol{R}(\boldsymbol{r}_j) = \begin{pmatrix} 1 & & \\ & c_\varphi & s_\varphi \\ & -s_\varphi & c_\varphi \end{pmatrix}\begin{pmatrix} -c_{\theta_j} & -s_{\theta_j} & \\ s_{\theta_j} & -c_{\theta_j} & \\ & & 1 \end{pmatrix},$$

Eq. (13) can be readily diagonalized in terms of the total angular momentum n_J

$$\boldsymbol{H}_{n_J}\begin{pmatrix} m_+(n_J) \\ m_-(-n_J) \end{pmatrix} = \boldsymbol{\sigma}_3\begin{pmatrix} m_+(n_J) \\ m_-(-n_J) \end{pmatrix}\overline{E},$$

with

$$m_\pm(n_J) \equiv \frac{1}{\sqrt{M}}\sum_{j=1}^{M} e^{i\frac{2\pi n_J}{M}j}m_\pm(\theta_j), \tag{22}$$

where n_J is defined modulo M $(n_J = 0,1,\ldots,M-1)$. $\boldsymbol{H}_{n_J}$ takes the form of

$$\boldsymbol{H}_{n_J} \equiv -M_s\alpha\boldsymbol{\sigma}_0 - M_s\begin{pmatrix} g_{++}(n_J) & g_{+-}(n_J) \\ g_{-+}(n_J) & g_{--}(n_J) \end{pmatrix},$$

with

$$\begin{aligned}\begin{pmatrix} g_{++}(n_J) & g_{+-}(n_J) \\ g_{-+}(n_J) & g_{--}(n_J) \end{pmatrix} &= -2iB_0(n_J)c_\varphi\boldsymbol{\sigma}_3 + \{A_0(n_J)(-2+3c_\varphi^2) - A_1(n_J) \\ &\quad\times(1+c_\varphi^2)\}\boldsymbol{\sigma}_0 - \{3A_0(n_J)c_\varphi^2 + A_1(n_J)(1-c_\varphi^2)\}\boldsymbol{\sigma}_1,\end{aligned}$$

and

$$A_0(n_J) \equiv \frac{\Delta V}{64\pi r^3}\sum_{j=1}^{M-1}e^{iq_Jj}\frac{1}{s^3_{\frac{\theta_j}{2}}},$$

$$A_1(n_J) \equiv \frac{\Delta V}{64\pi r^3}\sum_{j=1}^{M-1}e^{iq_Jj}\frac{1}{s_{\frac{\theta_j}{2}}},$$

$$B_0(n_J) \equiv \frac{i\Delta V}{64\pi r^3}\sum_{j=1}^{M-1}e^{iq_Jj}\frac{c_{\frac{\theta_j}{2}}}{s^2_{\frac{\theta_j}{2}}},$$

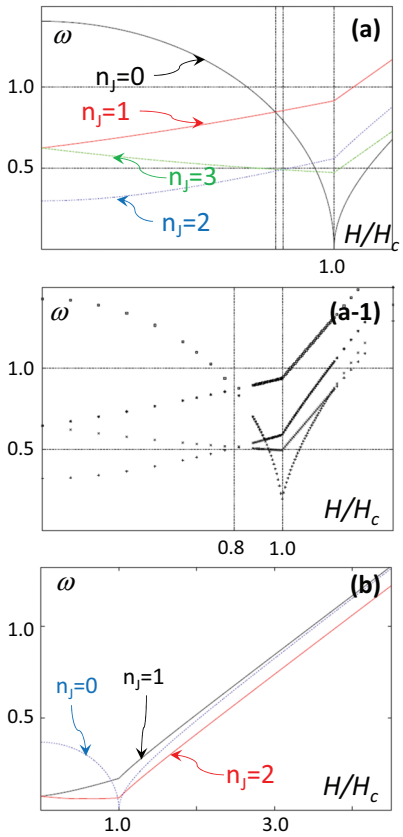

FIG. 8. (Color online) (a) Atomic-orbital levels as a function of the field in a single four-spin cluster case. Equation (13) is diagonalized, where the demagnetization field for each site (α) comes from the spins in the same cluster. The saturation field at which $n_J = 0$ becomes zero is around $H_c = 1.26$. The level inversion between $n_J = 1$ and $n_J = 0$ is around $H/H_c = 0.80$, while that between $n_J = 3$ and $n_J = 2$ is around $H/H_c = 0.83$. (a-1) Atomic-orbital levels as a function of the field calculated from Eq. (13) in the decorated square lattice model. Equation (13) is diagonalized, where the demagnetization field for each site includes not only those from the spins in the same cluster but also those from spins in the other cluster. The saturation field is around $H_c = 1.71$, where the level of $n_J = 0$ goes below the others. (b) Atomic-orbital levels as a function of the field (single three-spin cluster case) with $H_c = 0.32$.

with $q_J \equiv \frac{2\pi n_J}{M}$. Eigenfrequency with angular momentum n_J takes the following form in the particle space:

$$\varepsilon_{n_J} = M_s \lambda_{n_J} - 2c_\varphi M_s B_0(n_J) \tag{23}$$

with

$$\lambda_{n_J} \equiv \sqrt{[-\alpha + 2A_0(n_J) + 2A_1(n_J)]} \times \sqrt{\left[-\alpha + 2A_0(n_J) - 6A_0(n_J)c_\varphi^2 + 2A_1(n_J)c_\varphi^2\right]}.$$

Figures 8(a) and 8(b) show how the spin-wave excitations for a single cluster with $M = 4$ and $M = 3$, Eq. (23), behave as a function of the field respectively. In either case, doubly degenerate modes at the zero field, $n_J = 1$ and $n_J = M - 1$ ($p_\mp$-wave orbital respectively in the square-lattice case; see Fig. 11), are split on increasing the field, while that with $n_J = 0$ (s-wave orbital) decreases its resonance frequency, to reach zero at the saturation field $H = H_c$. Above the field, the s-wave atomic-orbital level increases again, to form a quasidegeneracy with the atomic-orbital level of $n_J = M - 2$ in the large field limit

$$\varepsilon_{n_J=0} = \varepsilon_{n_J=M-2} + \mathcal{O}(1/H). \tag{24}$$

The atomic-orbital levels shown in Figs. 8(a) and 8(b) are those for a single four- (three-)spin cluster, where the demagnetization field stems only from those spins in the same cluster. Even when demagnetization fields from surrounding clusters are included, which is the case with Eq. (13), the field dependence of the atomic-orbital levels behaves qualitatively in the same way as in Figs. 8(a) and 8(b). Namely, the decorated square-lattice model and honeycomb-lattice model respects the same fourfold (threefold) rotational symmetry as in the single four- (three-)spin cluster, so that only a value of the saturation field and specific expression for demagnetization field will be modified, e.g., compare Fig. 8(a) with Fig. 8(a-1).

From Figs. 8(a) and 8(a-1), notice that there appear a couple of level inversions between different atomic orbitals, such as the one between $n_J = 0$ and $n_J = 1$ around $H = 0.80H_c$, and the one between $n_J = 2$ and $n_J = 3$ around $H = 0.83H_c$. Now that one of these two atomic orbitals is always either $p_x + ip_y$ or $p_x - ip_y$-like orbital while the others are parity even, it is expected from its electron analog[25] that these level inversions endow the spin-wave volume-mode bands constructed from these atomic orbitals with nonzero Chern integers. In fact, a similar type of the band inversion plays a vital role in the emergence of nontrivial topological phases in quantum spin Hall insulators.[25,26]

B. TB model for the square lattice case

To clarify how the level inversion between atomic orbitals leads to spin-wave bands with nonzero Chern integers, we next construct from Eqs. (15)–(17) a tight-binding (TB) model for the decorated square lattice. $\boldsymbol{H}_0$ and corresponding $\boldsymbol{T}_0$ in Eqs. (16) and (17) are replaced by those for the single four-spin cluster. As for $\tilde{\boldsymbol{H}}_1$, only the nearest-neighbor hopping integrals are included. Such approximations may be justified, because the dipolar interaction decays as $1/R^3$ with R being a distance between two spins; an amplitude of the next-nearest-neighbor hopping is roughly $2\sqrt{2}$, 8, and $5\sqrt{5}$ times larger than those of the second, third, and fourth nearest-neighbor hopping integrals respectively. In fact, band dispersions for spin-wave volume-mode bands obtained from this short-ranged TB model show qualitatively good agreements with those shown in the previous section (compare Fig. 9 with Fig. 3). For example, all the sequences of the band touchings described in Sec. III are identified near similar field strengths, when scaled by the respective saturation fields; Fig. 9(a)–9(f). Correspondingly, the Chern integers for all the four spin-wave bands take the same sequence of the integer values as found in the previous section (Fig. 10). The comparison also suggests that the nonparabolic characters of a certain band dispersion around the Γ point in Fig. 3 stems from long-range hopping integrals in $\tilde{\boldsymbol{H}}_1$, i.e., long-range character of the magnetic dipolar interaction, which is consistent with the similar feature of the forward volume modes.[2]

The sequence of band touchings between the highest and the third lowest spin-wave band results from the level inversion

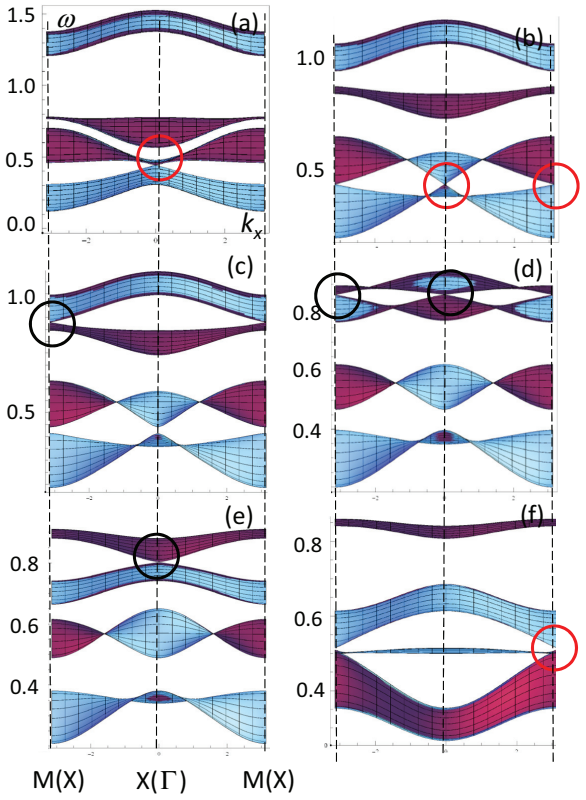

FIG. 9. (Color online) Side view of spin-wave band dispersions for decorated square-lattice model calculated from the tight-binding Hamiltonian, Eqs. (15)–(17) where only nearest-neighbor hopping integrals are included. As for atomic-orbital levels, Eq. (17), and the respective wave function $\boldsymbol{T}_0$ used in Eq. (16), we used those for the single four-cluster. (a) $H = 0.23H_c$, (b) $H = 0.66H_c$, (c) $H = 0.71H_c$, (d) $H = 0.79H_c$, (e) $H = 0.85H_c$, (f) $H = 1.4H_c$, where H_c denotes the saturation field for single four-spin cluster, [$H_c = 1.26$; see the caption of Fig. 8(a)]. At (a), (b), and (f), the lowest spin-wave band and the second lowest one form band touchings at Γ point, X points, and M point, respectively. At (c), (d), and (e), the highest spin-wave band and the third lowest one form band touchings at M point, X points, and Γ point, respectively.

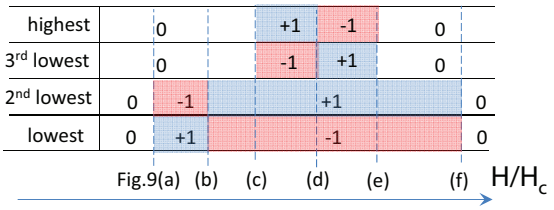

FIG. 10. (Color online) Chern integers for four spin-wave bands as a function of the field. (a)–(f) depicted in the figure correspond to the fields at which band touchings occur as shown in Figs. 9(a)–9(f), respectively. Note also that the third lowest spin-wave band at Fig. 9(e) is mainly composed of $n_J = 0$, while the second lowest and the lowest bands are mainly composed of $n_J = 2,3$. From (e) to (f), the former band goes below the latter two until $H = H_c$, while, for $H > H_c$. it increases its frequency again, in the same way as the s-wave atomic orbital does in Fig. 8(a). For clarity, we call the latter two as second lowest and lowest, even though they are not during (e)–(f).

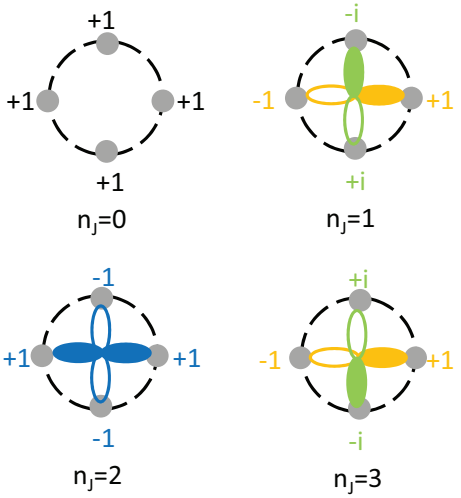

FIG. 11. (Color online) Shapes of the atomic orbitals in the decorated square lattice model. That of $n_J = 0$ is s-wave, while those of $n_J = 1,2,3$ are $p_x - ip_y$-wave, $d_{x^2-y^2}$-wave, and $p_x + ip_y$-wave respectively.

between the atomic orbital with $n_J = 1$ and that with $n_J = 0$ [Fig. 8(a)], while the other sequence between the lowest and second lowest spin-wave band is from those with $n_J = 2$ and $n_J = 3$ [Fig. 8(a)].

To see this, notice first that the atomic orbitals with $n_J = 0,1,2,3$ takes s-wave, $p_- \equiv p_x - ip_y$, $d_{x^2-y^2}$, and $p_+ \equiv p_x + ip_y$-wave orbitals respectively (Fig. 11). Namely, Eq. (22) suggests that atomic-orbital wave functions for $n_J = 1$ and $n_J = 3$ take imaginary values ('i') along the y direction, while taking real values along the x direction. Meanwhile, those for $n_J = 0$ and $n_J = 2$ always take real values; $n_J = 0$ takes $+1$ for x link and y link while $n_J = 2$ takes $+1$ and -1 for x link and y link, respectively. As a result, the nearest-neighbor interorbital hopping integral between $n_J = 1$ and $n_J = 0$ and that between $n_J = 2$ and $n_J = 3$ always become pure imaginary along the y link. In fact, using symmetry arguments, one can generally derive from Eqs. (18) and (19) a nearest-neighbor hopping model composed of $n_J = 0$ and $n_J = 1$ as

$$\begin{aligned}\hat{H}_{01} = &\sum_n (\varepsilon_0 \gamma^\dagger_{0,n}\gamma_{0,n} + \varepsilon_1 \gamma^\dagger_{1,n}\gamma_{1,n}) \\ &+ \sum_n \sum_{\mu=x,y} \sum_{\sigma=\pm} \left(a_{00}\gamma^\dagger_{0,n}\gamma_{0,n+\sigma e_\mu} + a_{11}\gamma^\dagger_{1,n}\gamma_{1,n+\sigma e_\mu}\right) \\ &+ \sum_n \sum_{\sigma=\pm} \left(\sigma b_{01}\gamma^\dagger_{0,n}\gamma_{1,n+\sigma e_x} + \text{H.c.}\right) \\ &+ \sum_n \sum_{\sigma=\pm} \left(-i\sigma b_{01}\gamma^\dagger_{0,n}\gamma_{1,n+\sigma e_y} + \text{H.c.}\right), \end{aligned} \tag{25}$$

with real valued a_{00}, a_{11} and b_{01}. We have ignored (or integrated out within the second-order perturbation) those hopping terms which involve $n_J = 2$ and $n_J = 3$ and those between the particle space and the hole space. Such approximations are justified, when the atomic-orbital level of $n_J = 0$ and that of $n_J = 1$ are proximate to each other and when it comes to those spin-wave bands near these levels.

The highest and the third lowest spin-wave bands around $H/H_c = 0.78 \sim 0.82$ are mainly composed of the atomic orbitals with $n_J = 0$ and $n_J = 1$ [compare Fig. 8(a) with Figs. 9(c)–9(e)] and thus can be approximately obtained from $\hat{H}_{01}$. The Hamiltonian in the momentum space takes the form[25,26]

$$\boldsymbol{H}_{01,\boldsymbol{k}} = \begin{pmatrix} \varepsilon_0 + 2a_{00}(c_{k_x} + c_{k_y}) & -2ib_{01}(s_{k_x} - is_{k_y}) \\ 2ib_{01}(s_{k_x} + is_{k_y}) & \varepsilon_1 + 2a_{11}(c_{k_x} + c_{k_y}) \end{pmatrix}, \tag{26}$$

with $(c_{k_x}, s_{k_x}) = (\cos k_x, \sin k_x)$, which gives momentum-frequency dispersions for the highest and the second highest spin-wave bands as

$$\mathcal{E}_{0,\boldsymbol{k}} \equiv \frac{\varepsilon_0 + \varepsilon_1}{2} + (a_{00} + a_{11})(c_{k_x} + c_{k_y}) + \frac{\Delta_{\boldsymbol{k}}}{2}, \tag{27}$$

$$\mathcal{E}_{1,\boldsymbol{k}} \equiv \frac{\varepsilon_0 + \varepsilon_1}{2} + (a_{00} + a_{11})(c_{k_x} + c_{k_y}) - \frac{\Delta_{\boldsymbol{k}}}{2}, \tag{28}$$

with

$$\Delta_{\boldsymbol{k}} \equiv \sqrt{\left[\varepsilon_0 - \varepsilon_1 + 2(a_{00} - a_{11})(c_{k_x} + c_{k_y})\right]^2 + 16b_{01}^2(s_{k_x}^2 + s_{k_y}^2)}. \tag{29}$$

The atomic-orbital level with $n_J = 0$ and that with $n_J = 1$ are inverted around $H = 0.80H_c$, where $\varepsilon_0 - \varepsilon_1$ changes its sign from positive to negative [Fig. 8(a)]. From their orbital shapes, the nearest-neighboring hopping integral between s-wave orbitals should be always positive $a_{00} > 0$, while that between p_--wave orbitals should be negative $a_{11} < 0$, which leads to $a_{00} - a_{11} > 0$. These two observations mean that, on increasing the field, the two bands given by Eqs. (27) and (28) first form a massless Dirac-cone spectrum at $\boldsymbol{k} = (\pi,\pi)$ (M point) when $\varepsilon_0 - \varepsilon_1 = 4(a_{00} - a_{11})$, then two massless Dirac-cone spectra at $\boldsymbol{k} = (\pi,0)$ and $\boldsymbol{k} = (0,\pi)$ (X point) when $\varepsilon_0 - \varepsilon_1 = 0$, and finally one massless Dirac spectrum at $\boldsymbol{k} = (0,0)$ when $\varepsilon_0 - \varepsilon_1 = -4(a_{00} - a_{11})$. The band touching at the M point is nothing but that in Fig. 9(c), those at the X points are those in Fig. 9(d), and that at Γ point corresponds to that in Fig. 9(e). In fact, analytic evaluations of Eq. (12) for Eq. (26) show that the Chern integer for the highest (third lowest) spin-wave band becomes $+1(-1)$ for $4(a_{00} - a_{11}) > \varepsilon_0 - \varepsilon_1 > 0$ and $-1(+1)$ for $0 > \varepsilon_0 - \varepsilon_1 > -4(a_{00} - a_{11})$, which is consistent with Fig. 10.

Similarly, the other sequence of band touchings formed by the lowest and second lowest spin-wave bands is explained in terms of the two-band models composed by $n_J = 3$ and $n_J = 2$ atomic orbitals

$$\boldsymbol{H}_{32,\boldsymbol{k}} = \begin{pmatrix} \varepsilon_3 + 2a_{33}(c_{k_x} + c_{k_y}) & -2ib_{32}(s_{k_x} - is_{k_y}) \\ 2ib_{32}(s_{k_x} + is_{k_y}) & \varepsilon_2 + 2a_{22}(c_{k_x} + c_{k_y}) \end{pmatrix}, \tag{30}$$

Note that $\varepsilon_3 - \varepsilon_2$ changes its sign from positive to negative near $H \simeq 0.83H_c$ [Fig. 8(a)], while $a_{33} - a_{22}$ being always negative. This means that, on increasing H, the lowest and second lowest spin-wave bands around $H \simeq 0.83H_c$ first form a massless Dirac-cone spectrum at $\boldsymbol{k} = (0,0)$ when $\varepsilon_3 - \varepsilon_2 = -4(a_{33} - a_{22})$, then two massless Dirac spectra at $\boldsymbol{k} = (\pi,0)$ and $\boldsymbol{k} = (0,\pi)$ when $\varepsilon_3 - \varepsilon_2 = 0$, and finally one massless Dirac spectrum at $\boldsymbol{k} = (\pi,\pi)$ when $\varepsilon_3 - \varepsilon_2 = 4(a_{33} - a_{22})$. The band touching at the Γ point is nothing but that in Fig. 9(a), those at the X points are those in Fig. 9(b), and that at M point corresponds to that in Fig. 9(f). Noting that b_{32} has the same sign as b_{01} (see Fig. 11), one can also see from the previous evaluation that the Chern integer for the second lowest (lowest) spin-wave band becomes $-1(+1)$ for $-4(a_{33} - a_{22}) > \varepsilon_3 - \varepsilon_2 > 0$ and $+1(-1)$ for $0 > \varepsilon_3 - \varepsilon_2 > 4(a_{33} - a_{22})$, which is consistent with Fig. 10.

C. TB model for the honeycomb-lattice case

In the decorated honeycomb-lattice model, we have observed in Sec. III a finite band gap between the lowest spin-wave band and second lowest one, which are connected by a dispersion of a chiral edge mode. The gap and chiral edge mode persists for a sufficiently large field H. Based on a tight-binding model, we will employ a perturbation analysis from the large field limit and argue that the gap closes at two inequivalent K points only in the limiting case ($|H| \to \infty$), where both the time-reversal symmetry and hexagonal spatial symmetry are effectively recovered. More accurately, we will show that an effective spin-wave Hamiltonian in the large field limit respects these two symmetries within the order of $\mathcal{O}(1)$, while it starts to break them from $\mathcal{O}(1/H)$. As a result, within the order of $\mathcal{O}(1)$, the lowest and second lowest spin-wave band compose massless Dirac spectra at the K points. Once the $\mathcal{O}(1/H)$ corrections are included, the time-reversal symmetry is broken and the hexagonal symmetry (C_{6v}) reduces to its subgroup symmetry (C_6), which leads to a finite band gap at the K points. These symmetry breakings also endow the two bands with a nonzero Chern integer with opposite signs, which results in the emergence of chiral edge mode within the band gap.

The perturbation analysis begins with a tight-binding Hamiltonian for the honeycomb lattice model, Eq. (15)

$$\tilde{\boldsymbol{H}}_0 + \tilde{\boldsymbol{H}}_1 = H\boldsymbol{\sigma}_0 + \lambda \boldsymbol{V}_1 + \lambda \boldsymbol{V}_2, \tag{31}$$

where $\boldsymbol{\sigma}_0$ is a 2×2 unit matrix in the particle-hole space and both $\boldsymbol{V}_1$ and $\boldsymbol{V}_2$ are on the order of $\mathcal{O}(1)$. For a bookkeeping, we put λ, which can be set to 1 from the outset [those terms with λ are $\mathcal{O}(1)$, those with λ^2 are $\mathcal{O}(1/H)$, and those with λ^3 are $\mathcal{O}(1/H^2)$, see below]. $\boldsymbol{V}_1$ consists of on-cluster atomic-orbital levels and hopping terms in the excitonic channel, while $\boldsymbol{V}_2$ consists only of those in the Cooper channel

$$\boldsymbol{V}_1 \equiv \tilde{\boldsymbol{H}}_0 - H\boldsymbol{\sigma}_0 + \begin{pmatrix} \boldsymbol{t}^{(+,+)} & \boldsymbol{0} \\ \boldsymbol{0} & \boldsymbol{t}^{(-,-)} \end{pmatrix},$$

$$\boldsymbol{V}_2 \equiv \begin{pmatrix} \boldsymbol{0} & \boldsymbol{t}^{(+,-)} \\ \boldsymbol{t}^{(-,+)} & \boldsymbol{0} \end{pmatrix}.$$

In the large field limit, all the spin-wave excitations reduce to the ferromagnetic resonance (FMR) with its resonance frequency being H. Once the $\mathcal{O}(1)$ corrections $(\boldsymbol{V}_1,\boldsymbol{V}_2)$ are included, the FMR resonance is expected to split into a couple of spin-wave bands whose bandwidth are at most on the order of unity. To see this situation, let us erase those terms in the Cooper channel within a given order accuracy in $1/H$, and derive an effective Hamiltonian only for the particle space.

With a matrix satisfying $\boldsymbol{\sigma}_3\boldsymbol{\rho}\boldsymbol{\sigma}_3 = \boldsymbol{\rho}^\dagger$, the transformed Hamiltonian takes the form

$$\begin{aligned}\boldsymbol{H}_{\rm eff} &\equiv e^{-i\lambda\boldsymbol{\sigma}_3\boldsymbol{\rho}\boldsymbol{\sigma}_3}\,(H+\lambda\boldsymbol{V}_1+\lambda\boldsymbol{V}_2)\,e^{i\lambda\boldsymbol{\rho}}\\ &= \left(1-i\lambda\boldsymbol{\sigma}_3\boldsymbol{\rho}\boldsymbol{\sigma}_3-\frac{\lambda^2}{2}\boldsymbol{\sigma}_3\boldsymbol{\rho}^2\boldsymbol{\sigma}_3+\cdots\right)\\ &\quad\times(H+\lambda\boldsymbol{V}_1+\lambda\boldsymbol{V}_2)\left(1+i\lambda\boldsymbol{\rho}-\frac{\lambda^2}{2}\boldsymbol{\rho}^2+\cdots\right)\\ &= H+\lambda\boldsymbol{V}_1+\lambda\boldsymbol{V}_2-\lambda i\boldsymbol{\sigma}_3\boldsymbol{\rho}\boldsymbol{\sigma}_3H+i\lambda H\boldsymbol{\rho}\\ &\quad-\frac{\lambda^2}{2}\boldsymbol{\sigma}_3\boldsymbol{\rho}^2\boldsymbol{\sigma}_3H-\frac{\lambda^2}{2}H\boldsymbol{\rho}^2+\lambda^2\boldsymbol{\sigma}_3\boldsymbol{\rho}\boldsymbol{\sigma}_3H\boldsymbol{\rho}\\ &\quad-i\lambda^2\boldsymbol{\sigma}_3\boldsymbol{\rho}\boldsymbol{\sigma}_3\boldsymbol{V}_1+i\lambda^2\boldsymbol{V}_1\boldsymbol{\rho}-i\lambda^2\boldsymbol{\sigma}_3\boldsymbol{\rho}\boldsymbol{\sigma}_3\boldsymbol{V}_2\\ &\quad+i\lambda^2\boldsymbol{V}_2\boldsymbol{\rho}+\mathcal{O}(\lambda^3).\end{aligned}\tag{32}$$

We choose ρ such that all the matrix elements in the Cooper channels will cancel each other within the order of $\mathcal{O}(1)$

$$\boldsymbol{V}_2 = i\boldsymbol{\sigma}_3\boldsymbol{\rho}\boldsymbol{\sigma}_3H-iH\boldsymbol{\rho},$$

or equivalently,

$$(\boldsymbol{\rho})_{n,\overline{m}} = i\frac{(\boldsymbol{V}_2)_{n,\overline{m}}}{2H},\ (\boldsymbol{\rho})_{\overline{n},m} = i\frac{(\boldsymbol{V}_2)_{\overline{n},m}}{2H},\tag{33}$$

where $\overline{n}$ is for the indices in the hole space and n is for those in the particle space; $(\boldsymbol{\sigma}_3)_{n,m} = \delta_{n,m}$ and $(\boldsymbol{\sigma}_3)_{\overline{n},\overline{m}} = -\delta_{n,m}$. With this rotated frame, all the matrix elements in the Cooper channel are at most on the order of $\mathcal{O}(1/H)$

$$\begin{aligned}\boldsymbol{H}_{\rm eff} &= H+\lambda\boldsymbol{V}_1-\frac{i\lambda^2}{2}(\boldsymbol{\sigma}_3\boldsymbol{\rho}\boldsymbol{\sigma}_3\boldsymbol{V}_2-\boldsymbol{V}_2\boldsymbol{\rho})\\ &\quad-i\lambda^2(\boldsymbol{\sigma}_3\boldsymbol{\rho}\boldsymbol{\sigma}_3\boldsymbol{V}_1-\boldsymbol{V}_1\boldsymbol{\rho}).\end{aligned}\tag{34}$$

The last two terms have matrix elements in Cooper channels. When we further rotate in the particle-hole space such that they will be set off by generated terms, these two terms simply result in higher-order terms, $\mathcal{O}(1/H^2)$, while the remaining terms are kept intact. We thus drop them by hand, to keep the first four terms as the effective Hamiltonian. On the substitution of Eq. (33) into Eq. (34), we then have the effective Hamiltonian to the order of $1/H$ as

$$\left(\boldsymbol{H}^{(2)}_{\rm eff}\right)_{n,m} = H\delta_{n,m}+(\boldsymbol{V}_1)_{n,m}+\frac{1}{2H}\sum_{\overline{p}}(\boldsymbol{V}_2)_{n,\overline{p}}(\boldsymbol{V}_2)_{\overline{p},m}.\tag{35}$$

The superscript (2) in the left-hand side denotes that the effective Hamiltonian is asymptotically exact within the second order in λ (or within the first order in $1/H$). The sum with respect to $\overline{p}$ is taken only over the hole space. From Eq. (35), one can readily see that, once the $\mathcal{O}(1)$ corrections $(\boldsymbol{V}_1)$ are included, the FMR resonance localized at H is split into a couple of spin-wave bands whose bandwidth are at most on the order of unity.

Within the order of $\mathcal{O}(1)$, the effective Hamiltonian derived so far is invariant under the time-reversal operation and hexagonal symmetry operations. To see this, let us focus on the first two terms of Eq. (35). With the atomic orbital index $(n_J = j,m)$ and cluster index (n,n') being made explicit, they take the following form

$$\left(\boldsymbol{H}^{(1)}_{\rm eff}\right)_{(j,n|m,n')} = \delta_{n,n'}\delta_{j,m}\varepsilon_j+\boldsymbol{t}^{(+,+)}_{(j,n|m,n')}.$$

In the leading order in $1/H$, the interorbital/intraorbital hopping integral between an orbital with $n_J = j$ at the nth cluster and that with $n_J = m$ at the n'th cluster is given by

$$\boldsymbol{t}^{(+,+)}_{(j,n|m,n')} = \sum_{\theta_l,\theta_{l'}} e^{i(j+1)\theta_l-i(m+1)\theta_{l'}}\frac{1}{6R^3}.\tag{36}$$

$\theta_{l^{(\prime)}}$ $(l^{(\prime)} = 1,2,3)$ in the right-hand side specifies a spatial location of a ferromagnetic spin within a cluster. Within a cluster that encompasses an A-sublattice site or B-sublattice site at (x_n,y_n), we take $\theta_l \equiv \frac{2\pi l}{3}$ or $\pi+\frac{2\pi l}{3}$, respectively, such that the location of the ferromagnetic spin is always given by $(x_n - r\sin\theta_l, y_n+\cos\theta_l)$. R denotes a spatial distance between a ferromagnetic spin specified by (θ_l,n) and that by $(\theta_{l'},n')$

$$R \equiv \left|\begin{pmatrix}x_n-r\sin\theta_l\\ y_n+r\cos\theta_l\end{pmatrix}-\begin{pmatrix}x_{n'}-r\sin\theta_{l'}\\ y_{n'}+r\cos\theta_{l'}\end{pmatrix}\right|.$$

Within the order of $\mathcal{O}(1)$, a complex conjugation of hopping integrals can be readily set off by a sign change of the orbital angular momentum $n_L \equiv n_J+1$. Namely, the complex conjugate of Eq. (36) is transformed to itself by a proper exchange between $n_L = +1$ $(n_J = 0)$ and $n_L = 2 \equiv -1 \pmod 3$ $(n_J = 1)$. This in combination with Eq. (24) indicates that the effective Hamiltonian up to the order of $\mathcal{O}(1)$ is invariant under the following time-reversal operation:

$$\left(\boldsymbol{H}^{(1)}_{\rm eff}\right)^*_{(j,n|m,n')} = \boldsymbol{Q}_{jj'}\left(\boldsymbol{H}^{(1)}_{\rm eff}\right)_{(j',n|m',n')}\boldsymbol{Q}^t{}_{m'm}\tag{37}$$

with a proper basis change

$$\boldsymbol{Q} \equiv \begin{pmatrix}&1&\\1&&\\&&1\end{pmatrix},$$

which exchanges $n_L = +1$ $(n_J = 0)$ and $n_L = -1$ $(n_J = 1)$, while keeping $n_L = 0$ $(n_J = 2)$ intact. It is also invariant under three mirror operations in the hexagonal symmetry, $\sigma_{v,1}$, $\sigma_{v,2}$, $\sigma_{v,3}$, π rotation C_2, and $\frac{2\pi}{3}$ rotation C_3,

$$\begin{aligned}\left(\boldsymbol{H}^{(1)}_{\rm eff}\right)_{(j,\sigma_{v,1}(n)|m,\sigma_{v,1}(n'))} &= \boldsymbol{Q}_{jj'}\left(\boldsymbol{H}^{(1)}_{\rm eff}\right)_{(j',n|m',n')}\boldsymbol{Q}^t{}_{m'm},\\ \left(\boldsymbol{H}^{(1)}_{\rm eff}\right)_{(j,\sigma_{v,2}(n)|m,\sigma_{v,2}(n'))} &= \boldsymbol{O}_{jj'}\left(\boldsymbol{H}^{(1)}_{\rm eff}\right)_{(j',n|m',n')}\boldsymbol{O}^\dagger{}_{m'm},\\ \left(\boldsymbol{H}^{(1)}_{\rm eff}\right)_{(j,\sigma_{v,3}(n)|m,\sigma_{v,3}(n'))} &= \boldsymbol{O}^\dagger{}_{jj'}\left(\boldsymbol{H}^{(1)}_{\rm eff}\right)_{(j',n|m',n')}\boldsymbol{O}_{m'm},\\ \left(\boldsymbol{H}^{(1)}_{\rm eff}\right)_{(j,C_2(n)|m,C_2(n'))} &= \left(\boldsymbol{H}^{(1)}_{\rm eff}\right)_{(j',n|m',n')},\\ \left(\boldsymbol{H}^{(1)}_{\rm eff}\right)_{(j,C_3(n)|m,C_3(n'))} &= \boldsymbol{P}^\dagger{}_{jj'}\left(\boldsymbol{H}^{(1)}_{\rm eff}\right)_{(j',n|m',n')}\boldsymbol{P}_{m'm},\end{aligned}$$

respectively with

$$\boldsymbol{O} \equiv \begin{pmatrix}&e^{-i\frac{2\pi}{3}}&\\ e^{i\frac{2\pi}{3}}&&\\&&1\end{pmatrix},\quad \boldsymbol{P} \equiv \begin{pmatrix}e^{i\frac{2\pi}{3}}&&\\&e^{-i\frac{2\pi}{3}}&\\&&1\end{pmatrix}.$$

$\sigma_{v,\nu}$ ($\nu = 1,2,3$) denotes the mirror operation with respect to the plane subtended by $\boldsymbol{e}_\nu$ ($\nu = 1,2,3$; see Fig. 1) and $\boldsymbol{e}_z$ (a unit vector normal to the plane), C_2 is the two-fold rotation, which exchanges A-sublattice and B-sublattice and C_3 is the three-fold rotation within the plane [see Fig. 1(b)].

Owing to the hexagonal symmetry, the lowest two spin-wave bands obtained from $\boldsymbol{H}^{(1)}_{\rm eff}$ comprise two massless Dirac spectra at two inequivalent K points. Once the $\mathcal{O}(1/H)$ corrections are included, e.g., $\varepsilon_0 \neq \varepsilon_1$, the time-reversal symmetry is lost and the hexagonal (C_{6v}) symmetry ($C_2, C_3, C_3^{-1}, \sigma_{v,1}, \sigma_{v,2}, \sigma_{v,3}, \sigma_{d,1}, \sigma_{d,2}, \sigma_{d,3}$) with $\sigma_{d,\nu} \equiv C_2 \cdot \sigma_{v,\nu}$ reduces to C_6 symmetry (C_2, C_3, C_3^{-1}). As a result, Dirac spectra at the K points acquire a finite mass, which gives to the lowest two bands nonzero Chern integers.

The Chern integers for the lowest two spin-wave bands can be evaluated from a nearest-neighboring (NN) TB model. From the symmetry point of view, the NN TB Hamiltonian in the momentum space reads

$$\boldsymbol{H}_{{\rm NNTB},\boldsymbol{k}} = \begin{pmatrix} \varepsilon_0 & & & \alpha_0 a_{0,\boldsymbol{k}} & \beta a_{1,\boldsymbol{k}} & \gamma_0 a_{2,\boldsymbol{k}} \\ & \varepsilon_1 & & \beta a_{2,\boldsymbol{k}} & \alpha_1 a_{0,\boldsymbol{k}} & \gamma_1 a_{1,\boldsymbol{k}} \\ & & \varepsilon_2 & \gamma_0 a_{1,\boldsymbol{k}} & \gamma_1 a_{2,\boldsymbol{k}} & \eta a_{0,\boldsymbol{k}} \\ \alpha_0 a^*_{0,\boldsymbol{k}} & \beta a^*_{2,\boldsymbol{k}} & \gamma_0 a^*_{1,\boldsymbol{k}} & \varepsilon_0 & & \\ \beta a^*_{1,\boldsymbol{k}} & \alpha_1 a^*_{0,\boldsymbol{k}} & \gamma_1 a^*_{2,\boldsymbol{k}} & & \varepsilon_1 & \\ \gamma_0 a^*_{2,\boldsymbol{k}} & \gamma_1 a^*_{1,\boldsymbol{k}} & \eta a^*_{0,\boldsymbol{k}} & & & \varepsilon_2 \end{pmatrix}$$

with

$$\begin{aligned} a_{0,\boldsymbol{k}} &\equiv e^{-i\boldsymbol{k}\boldsymbol{e}_1} + e^{-i\boldsymbol{k}\boldsymbol{e}_2} + e^{-i\boldsymbol{k}\boldsymbol{e}_3}, \\ a_{1,\boldsymbol{k}} &\equiv e^{-i\boldsymbol{k}\boldsymbol{e}_1} + e^{-i\frac{2\pi}{3}} e^{-i\boldsymbol{k}\boldsymbol{e}_2} + e^{i\frac{2\pi}{3}} e^{-i\boldsymbol{k}\boldsymbol{e}_3}, \\ a_{2,\boldsymbol{k}} &\equiv e^{-i\boldsymbol{k}\boldsymbol{e}_1} + e^{i\frac{2\pi}{3}} e^{-i\boldsymbol{k}\boldsymbol{e}_2} + e^{-i\frac{2\pi}{3}} e^{-i\boldsymbol{k}\boldsymbol{e}_3}. \end{aligned}$$

The first three columns and rows are for the three atomic orbitals encompassing an A-sublattice site, while the latter three are for those encompassing a B-sublattice site. ε_j stands for a level for an atomic orbital with $n_J = j$ ($j = 0,1,2$). α_0, α_1, β, η, γ_0 and γ_1 are NN interorbital or intraorbital (effective) transfer integrals, which can be evaluated from Eq. (35) up to $\mathcal{O}(1/H)$. It is clear from Eq. (36) that, within the order of $\mathcal{O}(1)$, $\gamma_0 = \gamma_1$, $\alpha_0 = \alpha_1$, and $\varepsilon_0 = \varepsilon_1$, which makes the lowest two bands form massless Dirac spectra at the K points [Fig. 12(b)]. A comparison between Figs. 12(a) and 12(b) suggests that the present NN TB Hamiltonian can qualitatively well reproduce the band structure of the lowest two bands in the large field limit, expect for a nonparabolic band structure of the lowest band near the Γ point.

Once finite $\Delta\gamma \equiv \gamma_0 - \gamma_1$, $\Delta\alpha \equiv \alpha_0 - \alpha_1$, and $\Delta\varepsilon \equiv \varepsilon_0 - \varepsilon_1$ are included, the exchange between $n_L = +1$ and $n_L = -1$ changes the signs of these terms, so that the time-reversal symmetry is broken and the hexagonal symmetry reduces to the C_6 symmetry. These symmetry reductions give a finite mass to the Dirac spectra. The mass can be evaluated from 2×2 Dirac Hamiltonians for the lowest two spin-wave bands, which can be obtained via $k \cdot p$ perturbation around these K points,

$$\boldsymbol{H}^{2\times 2}_{\boldsymbol{k}=\boldsymbol{K}+\boldsymbol{p}} = \frac{1}{2}\left(\Delta\varepsilon\ \sin^2\frac{\theta}{2} - 3\Delta\gamma\ \sin\theta\right)\boldsymbol{\sigma}_3 + \frac{3}{2}\left(\eta\ \cos^2\frac{\theta}{2} - \beta\ \sin^2\frac{\theta}{2}\right)(p_x\boldsymbol{\sigma}_1 - p_y\boldsymbol{\sigma}_2),$$

and

$$\boldsymbol{H}^{2\times 2}_{\boldsymbol{k}=\boldsymbol{K}'+\boldsymbol{p}} = -\frac{1}{2}\left(\Delta\varepsilon\ \sin^2\frac{\theta}{2} - 3\Delta\gamma\ \sin\theta\right)\boldsymbol{\sigma}_3 + \frac{3}{2}\left(\eta\ \cos^2\frac{\theta}{2} - \beta\ \sin^2\frac{\theta}{2}\right)(-p_x\boldsymbol{\sigma}_1 - p_y\boldsymbol{\sigma}_2),$$

with

$$\tan\theta \equiv 3\frac{\gamma_1 + \gamma_2}{\varepsilon_0 - \varepsilon_1}.$$

From these Hamiltonians, the Chern integers for the lowest and second lowest spin-wave bands are evaluated to be σ and $-\sigma$ respectively with

$$\sigma \equiv {\rm sign}\left(\Delta\varepsilon\ \sin^2\frac{\theta}{2} - 3\Delta\gamma\ \sin\theta\right).$$

A substitution of actual numbers into the parameters in the right-hand side shows that $\sigma = 1$, which is consistent with previous numerical evaluations in Sec. III. The nonzero Chern integers for the lowest two spin-wave bands results in an edge mode with the anticlockwise propagation, which has a chiral dispersion between these two bands.

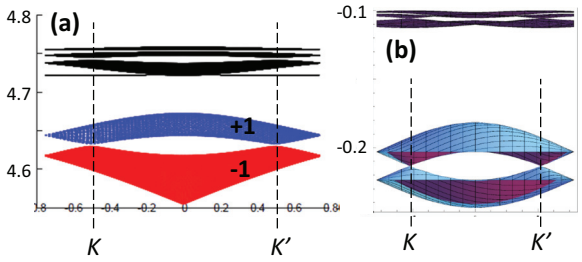

FIG. 12. (Color online) (a) Side view of spin-wave band dispersions for the decorated honeycomb-lattice model under a sufficiently strong field ($H = 5.0$). Because of a small but finite band gap at two K points, the Chern integers for the lowest two bands are -1 and $+1$ respectively. (b) Side view of spin-wave band dispersions calculated from the effective Hamiltonian to the order of $\mathcal{O}(1)$. For the atomic-orbital levels, we use those for a single three-spin cluster. To evaluate the nearest-neighbor hopping integral within the order of $\mathcal{O}(1)$, we use Eq. (36). When $H = 5.0$ is added, the resonance frequencies of the spin-wave bands in Fig. 12(b) become comparable to those in Fig. 12(a).

VI. MICROMAGNETIC SIMULATION

To uphold the existence of proposed chiral spin-wave edge mode by a standard method in the field, we perform a micromagnetic simulation by solving numerically the Landau-Lifshitz-Gilbert equation for the square-lattice model. We calculate magnetization dynamics by employing the fourth-order Runge-Kutta method with a time step $\Delta t = 1$ ps. Figure 13 schematically shows an entire system studied in

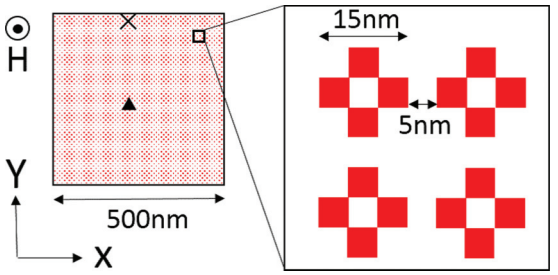

FIG. 13. (Color online) Schematic view of a simulated system that comprises ferromagnetic nanograin. Although we took the size of the ferromagnetic nanograin to be $5 \times 5 \times 5$ nm^3 as a demonstration, the present simulation is scale free. In the beginning of the simulation, we apply a pulse field either at the center (marked by a black triangle) or around the boundary (marked by a black cross).

the present micromagnetic simulation. It consists of four ferromagnetic nanograins in the unit cell. Although we took the size of the ferromagnetic nanograin to be $5 \times 5 \times 5$ nm^3 as a demonstration, the system is scalable; the simulation does not include any short-range exchange interactions. The saturation magnetization and Gilbert damping coefficient of the ferromagnetic grain are $1.75\mathrm{J}/\mu\mathrm{m}$ and 1.0×10^{-5} respectively. We regard each nanograin as a uniform magnet, to assign single spin degrees of freedom to each nanograin. Different ferromagnetic nanograins are coupled with one another through the magnetic dipolar interaction. The simulated system ($0 < X < L$ and $0 < Y < L$, Fig. 13) includes 25×25 unit cells. Without the field, the magnetization of each grain lies within the plane due to the dipolar interaction. Under a large out-of-plane DC field ($H_{\mathrm{dc}} > 4700$ Oe), the magnetization becomes fully polarized along the z direction. We took $H = 1.02H_c$ in the present simulation.

In order to excite spin-wave modes in a broad frequency range, we apply a pulsed magnetic field within a plane with its pulse time $t_{\mathrm{p}} = 1$ ps and its amplitude $H_{\mathrm{p}} = 1.0 \times 10^{-4}$ Oe. The pulse is applied locally at the center and around an edge of the system for the purpose of exciting volume modes and edge modes, respectively. After calculating a time evolution of the magnetization in the system, we take a Fourier transformation of the transverse moment, $m_+(X,Y,t) \equiv m_x(X,Y,t) + \mathrm{i}m_y(X,Y,t)$, with respect to time

$$s_+(X,Y,\omega) \equiv \sum_{j=0}^{n-1} m_+(X,Y,j\Delta T)\exp(2\pi \mathrm{i}\omega j \Delta T) \qquad (38)$$

with $\Delta T = 50$ ps and $n = 1024$. The frequency power spectrum, $\sum_{X,Y} |s_+(X,Y,\omega)|$, obtained by the pulse at the center and that by the pulse at the edge are shown in Fig. 14(a) separately. Spatial distributions of spin-wave excitations, $|s_+(X,Y,\omega)|$, for each case with different frequencies ω are shown in Figs. 14(b)–14(g). From them, one can see that the spin-wave volume modes and edge modes are selectively excited, depending on whether the initial pulse field is applied at the center or at the edge respectively. In the case of the pulse field at the center, we observe two band gaps for volume modes; one from 24 GHz to 30 GHz and the other from 37 GHz to 46 GHz. In the case of the pulse at the edge, we observed spin-wave edge modes mainly from 24 GHz to 42 GHz.

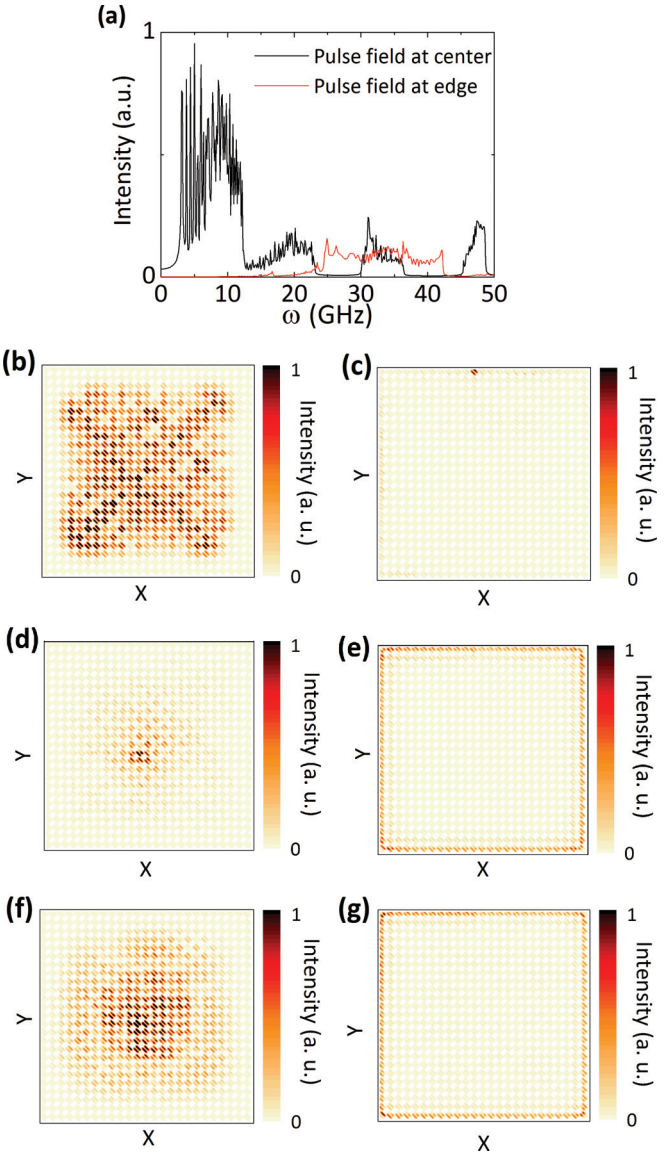

FIG. 14. (Color online) Fourier power spectra of magnetization dynamics. (a) Frequency dependence of the intensity of spin-wave excitations (see text). (b)–(g) Spatial distribution of the intensity, which is obtained by the application of the pulse field at center (b), (d), (f) and the edge (c), (e), (g); (b), (c) $\omega = 10$ GHz, (d), (e) $\omega = 29$ GHz, and (f), (g) $\omega = 31$ GHz.

A key feature of proposed chiral spin-wave edge mode is a unidirectional propagation of spin-wave densities, which is clarified by its frequency-wavelength dispersion relation. To obtain such a dispersion relation, we next take a Fourier transformation of the transverse moment with respect to both space and time. In order to compare the result with Figs. 4 and 5, we integrate the amplitude of the Fourier component with respect to the Y component of the momentum,

$$A(k_x,\omega) = \sum_{k_y} |s_+(k_x,k_y,\omega)|,$$

$$s_+(k_x,k_y,\omega) = \sum_{X,Y} s_+(X,Y,\omega)\ \exp(\mathrm{i}k_x X)\exp(\mathrm{i}k_y Y).$$

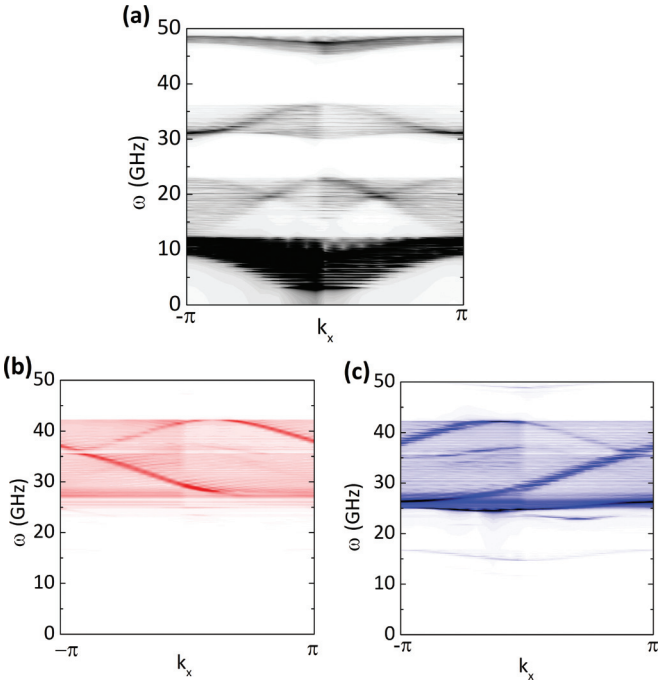

FIG. 15. (Color online) Dispersion relations of spin-wave modes. (a) Dispersion relation obtained by the application of the pulse field at the center. (b), (c) Dispersion relation obtained by the pulse at the edge. The Fourier transformation is taken only over the upper side ($Y > L/2$) for (b) and over the lower side ($Y < L/2$) for (c).

A contour plot of $A(k_x,\omega)$ as a function of k_x and ω gives a dispersion relation for spin-wave modes. Figure 15(a) shows the dispersion relation for the case of applying the pulse field at the center. It resembles those for spin-wave volume modes obtained in the preceding model calculation at the same parameter regime [Fig. 3(e)]. Figures 15(b) and 15(c) show the dispersion relations for the case of applying the pulse field at the edge. To clarify propagation directions of those two spin-wave edge modes running along the opposite boundaries of the system, we take the Fourier transformation only over the upper (or lower) side of the sample $L/2 < Y < L$ (or $0 < Y < L/2$); the one for the upper side is shown in Fig. 15(b), while the one for the lower is in Fig. 15(c). Both figures clearly indicate the existence of two counterpropagating chiral dispersions, each of which runs across any line of $\omega = \omega_0$ (25 GHz $< \omega_0 <$ 35 GHz) once and only once. The results also suggest an existence of another spin-wave edge mode from 35 GHz to 42 GHz, which has a quasiparabolic dispersion. Both of these edge modes in combination with volume modes shown in Fig. 15(a) are consistent with the dispersion relations for spin-wave modes obtained in the preceding model calculation at the same parameter regime [Figs. 5(a) and 5(a-1)].

When the Gilbert damping coefficient becomes larger, unidirectional propagations of spin density along the chiral spin-wave edge mode decay faster. Figure 16 shows spatial distributions of Fourier power spectra of magnetization dynamics, $|s_+(X,Y,\omega)|$, in the presence of larger Gilbert damping term ($\alpha = 0.001, 0.01$), where the initial pulse field is applied at the edge (Fig. 13) and the frequency is chosen within the band gap ($\omega = 29$ GHz). The results suggest that the coherence length

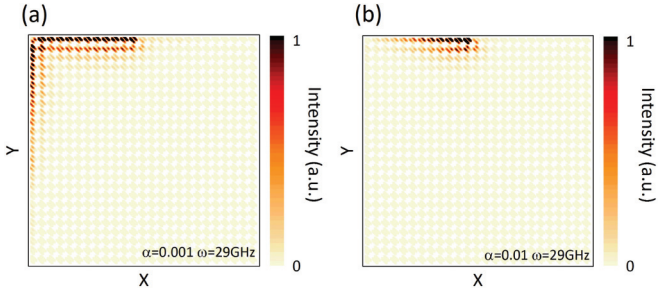

FIG. 16. (Color online) Spatial-resolved Fourier power spectra of magnetization dynamics in the presence of stronger dissipation. Spatial distribution of the intensity at $\omega = 29$ GHz, which is obtained by the application of the pulse field at the edge. (a) $\alpha = 0.001$, (b) $\alpha = 0.01$.

is roughly 25 unit cell size (500 nm) for $\alpha = 0.001$ and 8 unit cell size (160 nm) for $\alpha = 0.01$.

VII. SUMMARY, DISCUSSION, AND OPEN ISSUES

In this paper, we introduced two simple magnetic thin-film models, in which ferromagnetic nanoislands on periodic arrays are coupled with each other via magnetic dipolar interaction. Under the field applied perpendicular to the two-dimensional plane, spin-wave excitations in the systems have a chiral spin-wave edge mode localized at the boundaries of the systems, whose dispersion runs across a band gap for spin-wave volume modes. The sense of the rotation of the chiral edge mode is determined by a sign of the Chern integer for a spin-wave volume-mode band below the band gap.

To have volume-mode bands with finite Chern integers, we generally need multiple-band degrees of freedom within a unit cell. To this end, we considered two periodic arrays of ferromagnetic particles; decorated square-lattice model and honeycomb-lattice model. For the decorated square-lattice model, we observed that on increasing the out-of-plane field, there appears a sequence of band touchings between pairs of neighboring volume-mode bands. Owing to these band touchings, the Chern integers for the volume modes change their signs and, concomitantly, the chiral edge mode changes its sense of rotation from clockwise to anticlockwise or vice versa. For the decorated honeycomb-lattice model, we observed a finite band gap between the lowest spin-wave volume-mode band and second lowest spin-wave band, which are connected by a chiral dispersion of an edge mode. Though its sense of rotation is unchanged by the strength of the field in the honeycomb-lattice case, the gap and the chiral edge mode persists for a sufficiently large field.

To interpret these results, we next construct tight-binding descriptions for the linearized Landau-Lifshitz equation, in which atomic orbitals such as s-wave, $p_\pm$-wave, and $d_{x^2-y^2}$-wave orbitals are introduced within each unit cell. Among other, complex-valued characters in the $p_\pm$-wave orbitals break both the time-reversal symmetry and mirror symmetries of the models. These symmetry breakings lead to a nonzero Chern integer for spin-wave volume-mode bands and associated chiral spin-wave edge modes. Using this tight-binding model, we argue that the level inversions among different atomic orbital levels give rise to the so-called inverted

spin-wave bands with nonzero Chern integers. Our tight-binding analysis for the square-lattice model gives quantitative criteria for the emergence of finite field ranges within which spin-wave volume-mode bands have nonzero Chern integers.

For the decorated honeycomb-lattice model, we employ a perturbation analysis, starting from the large field limit. The analysis suggests that the effective Hamiltonian in the large field limit always respects time-reversal symmetry and the hexagonal symmetry within the order of $\mathcal{O}(1)$. Due to the mirror operations in the hexagonal symmetry, the lowest two spin-wave bands form gapless Dirac-cone spectra at two inequivalent K points. Once $\mathcal{O}(1/H)$-order corrections are included, however, the time-reversal symmetry is lost and hexagonal symmetry reduces to its abelian subgroup having no mirror symmetries. As a result, the gapless Dirac-cone spectra acquire a finite mass of the order of $\mathcal{O}(1/H)$, which leads to nonzero Chern integer for the two lowest spin-wave bands. This argument explains why the spin-wave volume-mode bands with nonzero Chern integers and associated chiral spin-wave edge mode persists in a very wide range of the field in the decorated honeycomb-lattice model.

Since a state-of-the-art sample production does not necessarily guarantee perfect periodic structurings, considering disorder effects associated with the lattice periodicity are experimentally relevant, which can be speculated from well-established knowledge of integer quantum Hall physics.[12,14,27,28] The effects are twofold. When the strength of the disorders is smaller than a characteristic frequency scale of the band gap, those volume modes near the band gap become localized due to the disorders, while chiral edge mode itself is free from these weak disorders. As a result, the frequency regime for the chiral spin-wave edge mode becomes even wider than that in the clean limit. When the strength of the disorders is increased to be larger than the scale of the band gap in the clean limit, the mobility gap closes and reopens. After the reopening the gap, the topological chiral edge mode disappears.[12,27,28] The proposed chiral spin-wave edge mode is also robust against the boundary shape; the edge modes persist in almost arbitrary shapes of the boundary, provided that the edge mode in the boundary has no interference with the other mode running along the opposite sample boundary.[14,15]

It is also a nontrivial issue whether submicrometer-scale ferromagnetic islands behave as a single spin or not. In preceding experimental systems mentioned before,[18,19] nonisotropic shapes of ferromagnetic islands give rise to strong magnetic dipolar anisotropies, forcing all the spins in each island to point along a same direction. In our model calculations, magnetic anisotropies within each island are not included from the outset. It is interesting to include these magnetic dipolar anisotropies into the present Landau-Lifshitz equation phenomenologically as the single-ion-type magnetic anisotropies. It is also equally likely that a ferromagnetic island has a couple of low-frequency relevant modes having different spin textures within the island. Such modes can be also utilized as a kind of atomic orbital, so that a system with only one ferromagnetic island within a unit cell could also have a chance to provide a volume-mode bands with finite Chern integers. Exploring such systems is, however, beyond the scope of the present paper and we leave them for future open issues.[20]

ACKNOWLEDGMENTS

We would like to thank Y. Suzuki, S. Miwa, and J. Feng for helpful discussions. This work is supported in part by Grant-in-Aids from the Ministry of Education, Culture, Sports, Science and Technology of Japan (Grants No. 21000004, No. 22540327, No. 23740225 and No. 24740284) and by a Grant for Basic Scientific Research Projects from the Sumitomo Foundation.

[1] R. W. Damon and J. R. Eshbach, J. Phys. Chem. Solids **19**, 308 (1961).
[2] R. W. Damon and H. Van De Vaart, J. Appl. Phys. **36**, 3453 (1965).
[3] B. A. Kalinikos and A. N. Slavin, J. Phys. C: Solid State Phys. **19**, 7013 (1986).
[4] V. V. Kryuglyak, S. O. Demokritov, and D. Grundler, J. Phys. D **43**, 264001 (2010).
[5] A. A. Serga, A. V. Chumak, and B. Hillebrands, J. Phys. D **43**, 264002 (2010).
[6] B. Lenk, H. Ulrichs, F. Garbs, and M. Münzenberg, Phys. Rep. **507**, 107 (2011).
[7] Yu. V. Gulyaev *et al.*, JETP Lett. **77**, 567 (2003).
[8] N. Singh, S. Goolaup, and A. O. Adeyeye, Nanotechnology **15**, 1539 (2004).
[9] C. C. Wang, A. O. Adeyeye, and N. Singh, Nanotechnology **17**, 1629 (2006).
[10] A. O. Adeyeye and N. Singh, J. Phys. D: Appl. Phys. **41**, 153001 (2008).
[11] R. Shindou, R. Matsumoto, S. Murakami, and Ohe J-i, arXiv:1204.3349.
[12] R. E. Prange and S. M. Girvin, ed., *The Quantum Hall Effect* (Springer-Verlag, Berlin, 1990).
[13] D. J. Thouless, M. Kohmoto, M. P. Nightingale, and M. den Nijs, Phys. Rev. Lett. **49**, 405 (1982).
[14] B. I. Halperin, Phys. Rev. B **25**, 2185 (1982).
[15] Y. Hatsugai, Phys. Rev. Lett. **71**, 3697 (1993).
[16] M. Karplus and J. M. Luttinger, Phys. Rev. **95**, 1154 (1954).
[17] M. Onoda and N. Nagaosa, J. Phys. Soc. Jpn. **71**, 19 (2002).
[18] R. F. Wang, C. Nisoli, R. S. Freitas, J. Li, W. McConville, B. J. Cooley, M. S. Lund, N. Samarth, C. Leighton, V. H. Crespi, and P. Schiffer, Nature (London) **439**, 303 (2006).
[19] C. A. Ross, M. Hwang, M. Shima, J. Y. Cheng, M. Farhoud, T. A. Savas, H. I. Smith, W. Schwaracher, F. M. Ross, M. Redjdal, and F. B. Humphrey, Phys. Rev. B **65**, 144417 (2002).
[20] Shindou, R. Ohe J-i *et al.* (unpublished).
[21] J. H. P. Colpa, Physica A **93**, 327 (1978).
[22] F. Bloch, Zeitschrift für Physik **61**, 206 (1930).
[23] T. Holstein and H. Primakoff, Phys. Rev. **58**, 1098 (1940).
[24] P. W. Anderson, Phys. Rev. **86**, 694 (1952).
[25] B. A. Bernevig, T. L. Hughes, and S. C. Zhang, Science **314**, 1757 (2006).
[26] L. Fu and C. L. Kane, Phys. Rev. B **76**, 045302 (2007).
[27] H. Aoki and T. Ando, Phys. Rev. Lett. **54**, 831 (1985).
[28] M. Onoda and N. Nagaosa, Phys. Rev. Lett. **90**, 206601 (2003).